BOUNDARY LAYER CONTROL BY MEANS OF DBD PLASMA ACTUATORS

Bachelor in Aerospace Engineering

Department of Aerospace Engineering
Universidad Carlos III de Madid

Author: Pablo Lechuga Capracci
Supervisor: Prof. Yacine Babou

June 2017

Abstract

In this thesis a new aerodynamic model to simulate the effect of Dielectric Barrier Discharge actuators on boundary layer control has been studied. The model has been implemented using commercial computational fluid dynamics software through built in tools that enables the inclusion of the body force created by the DBD model.

This model was further investigated by studying the influence of certain parameters to the velocity profile induced by the body force when a single actuator is placed over a flat plate in no-flow configuration and free boundary conditions.

Moreover, the model in nominal configuration was applied to a cylinder exposed to an incoming flow in order to assess its effect on the wake instability reduction. The actuators were applied by pairs and holding symmetry with respect to the x axis. The model proved to reduce drag, turbulence and oscillation amplitude. The influence of the incoming velocity to the drag reduction was obtained, finding a maximum velocity of 20 m/s for a single pair of actuators. From this value on, no significant effect is produced. The influence of the angle of application was also studied, finding the optimal angle of application at 82.5 degrees for an incoming velocity of 5 m/s and a body force of 0.015 N/m. The velocity evolution with time was deeply studied and results show high level of agreement with experimental findings in terms of wake mitigation.

Contents

List of Figures

List of Tables

Chapter 1

Introduction

Boundary Layer control is of high relevance within the aerodynamic and stability scopes due to the detrimental effects of separation such as reduction of lift and increase of drag on and aerodynamic surface, buffeting phenomena or noise generation. Flow separation problematics not only affect normal airfoils and wing surfaces but also extends to internal blades, ducts and diffusers.

Different innovative flow control methods and strategies are under investigation. In the recent years, interest has sparked for Electro Hydrodynamic (EHD) actuators, which promise instant actuation with low power consumption.

1.1 State of the art

Boundary layer control methods can be splitted in two categories:

- Passive methods which uses the properties of the body shapes.
- Active methods, through which the properties of the fluid are directly acted on without changing the surface. This methods includes the use of mechanical means, like flaps; and electrical systems, like the use of MEMS (Micro-electro-mechanical systems) and Electro-hydrodynamic (EHD) actuators.

Although mechanical devices may be effective, they have some drawbacks. They are complicated, add weight, have volume and are sources of noise and vibration. Moreover, they are composed of mechanical parts that wear away and that may break down.

Airflow actuation mechanism using electrical discharge (or plasma) is based on an efficient momentum transfer to the neutral species through collisions with ions produced and accelerated by the applied external electrical field. As a result, a macroscopic body force is generated and pushes the fluid in the vicinity of the plasma. In other words, using EHD actuation, a body force is induced to the flow through a conversion mechanism from electrical to mechanical power. Flow control systems based on EHD actuation have the following advantages:

- There are no moving mechanical parts
- High time response

- Flush mountable
- Easy to implement
- Low cost

For these reasons, plasma actuators development is a current challenging task in full expansion. The most promising actuator currently being investigated is the Dielectric Barrier Discharge (DBD) plasma actuators, as they proved for more than one decade its effectiveness [10]. Up to now, only partial models have been developed to describe the working principle of this actuators [7][14][11][5].

The exact modelling of DBD's is not tractable due to the high coupling between Naviere-Stokes equations for fluids, Poisson equations for electrostatics and the different species taking place in the problem, such as negative and positive ions or electrons. For this reason there is a need for a simpler model.

In the literature, some simpler models have been documented for easy implementation to commercial CFD solver.[13][12]

From the work of L. del Amo [1] and E. Nieto [8], an improved model (Merged model from now on) has been tested and demonstrated to have a fair fidelity for steady condition, being applied and validated in very diverse geometries and configurations. Nevertheless, regarding the performance of this model, there are many aspects that can be further investigated. For example:

- Model parameters' effect: The model to be implemented depends explicitly in the frequency and voltage applied to the actuator, together with the dielectric thickness. Moreover, there are several design parameters that depends implicitly on the arrangement settings. One aim of the present project is to assess the sensitivity of the model to this design parameters in order to obtain velocity profiles more faithful to experimental results.
- Application to time dependent and complex geometry simulations: Once the steady regime is deeply studied and the results show fair fidelity, the next step is to implement the model in time dependent simulations in order to assess its performance in aeronautical application.

The present project is motivated by this two points.

1.2 Objective

Taking this background into account, the motivation of this project is to asses the performance of the improved model implemented into a CFD software to numerically simulate the influence of DBD plasma actuators on flow control in realistic situations.

An analysis on how to tune the control parameters included in the Merged model will be provided in order to perform simulations with a higher fidelity to reality.

Later on, the flow over a cylinder will be studied to assess the influence of the actuators to act on the Von Kármán instability.

Chapter 2

Backround: DBD applied to a cylinder

2.1 Boundary layer separation

The boundary layer is an important concept which refers to the layer of fluid in the immediate vicinity of a bounding surface where the effects of viscosity are significant. Within this layer, velocity goes from zero, for the fluid in direct contact with the surface, to the upstream velocity at a characteristic boundary layer thickness δ.

In order to grasp the concept of boundary layer separation, consider the flow about a blunt body as sketched in Figure 2.1. According to Bernouilli's equation, the peak pressure on the body surface is reached at the front and rear stagnation points. As we move along the surface in the x direction, the velocity increases with the corresponding pressure decrease, producing a favorable pressure gradient until the top point is reached. From then on, the phenomena is exactly the opposite: the velocity decreases and the pressure increases leading to an adverse pressure gradient. The velocity in the wall vicinity is more sensitive to this adverse pressure gradient and in this region the velocity ends up being negative, generating a region of reversed flow, indicative of the separation of the boundary layer.[6]

When considering the flow over a cylinder, the separation of the boundary layer produces an unsteady phenomena called Von Kármán instability.

2.2 Von Kármán instability

In fluid dynamics, a von Kármán vortex street is a repeating pattern of swirling vortex shedding caused by the unsteady separation of flow of a fluid around blunt bodies. This vortex shedding is an oscillating flow that takes place when a fluid such as air or water flows past a bluff body at certain velocities, depending on the size and shape of the body. In this flow, vortices are created at the back of the body and detach periodically from either side of it. The fluid flow past the object creates alternating low-pressure vortices on the downstream side of the object. The object will tend to move toward the low-pressure zone.

This phenomena is of huge importance in engineering field because if the bluff structure is not mounted rigidly and the frequency of vortex shedding matches the resonance frequency of the structure,

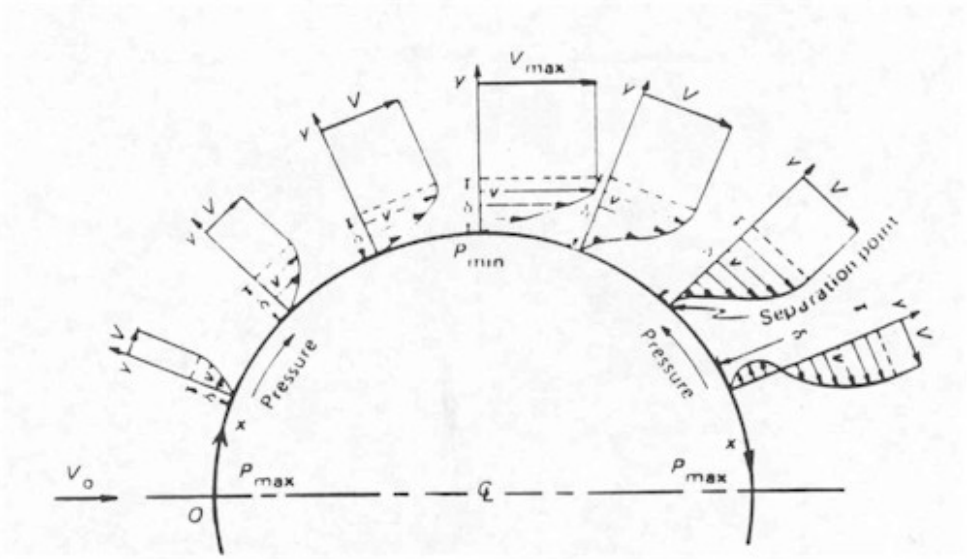

Figure 2.1: [9] Flow separation due to adverse pressure gradient.

it can begin to resonate, vibrating with harmonic oscillations driven by the energy of the flow. For this reason it is important for engineers to account for the possible effects of vortex shedding when designing a wide range of structures, from submarine periscopes to industrial chimneys and skyscrapers. In addition, this phenomena increases the drag and noise created by the body exposed to the flow, which have great importance in the aeronautical field.

Figure 2.2: Von Karman effect for low Re

It is important to highlight that the von Kármán instability behaviour has a strong dependence on the Reynolds number. This dependence is summarized in the following Figure 2.3.

Along this project, a wide range of Reynolds numbers will be considered, from 6000 to 20000. For this reason, and as shown in Figure 2.3, the vortex street is fully turbulent. A specific section included in next chapter will discuss about the turbulent model implemented in the CFD software in order to obtain physical results.

2.3 Operational principle of Surface DBD plasma actuators

In the present work, the possibility of mitigating the Von Kármán effect on a cylinder will be explored through a time dependent simulation. This will be done by the implementation of the Merged model

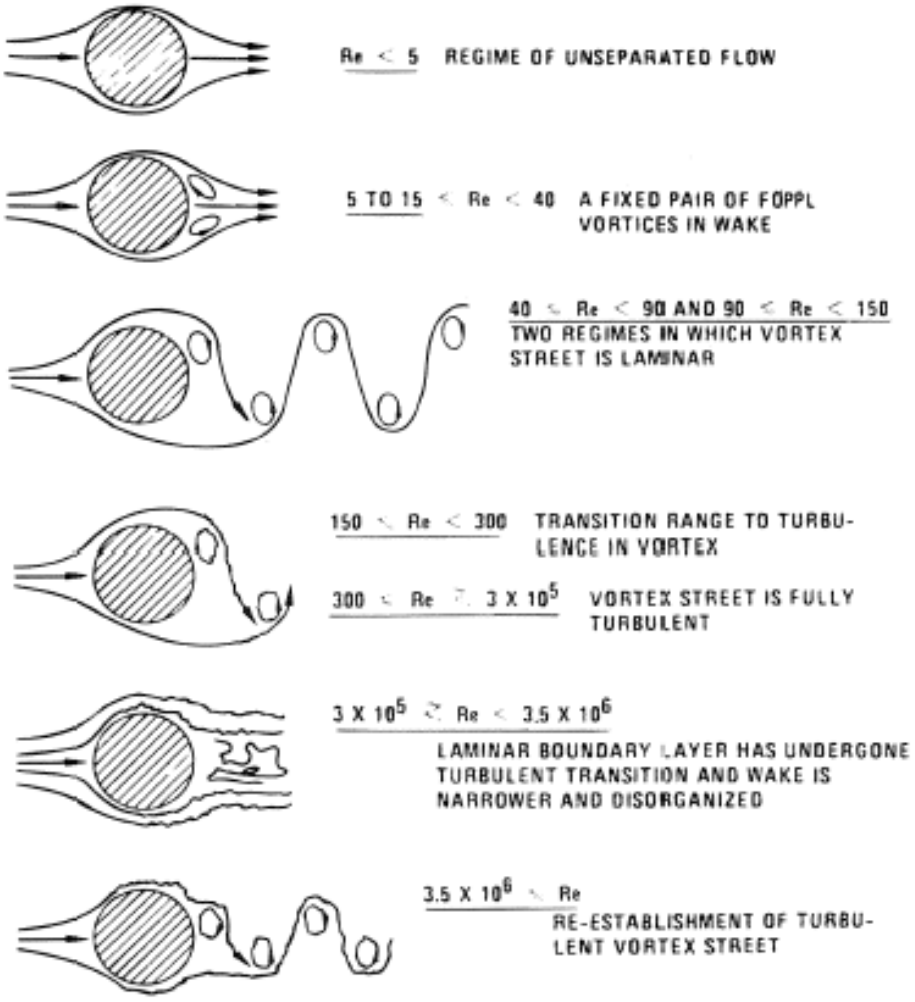

Figure 2.3: [3] Von Karman effect for varying Reynolds number

which simulates the effect of a Dielectric Barrier Discharge (DBD). Its operational principle is here-after explained.

A SDBD (Surface Dielectric Barrier Discharge) plasma actuator is arranged as two electrode plates displayed in asymmetrical manner, one above a dielectric surface and the other buried below it, integrated or encapsulated. The second electrode is usually placed right after the end of the upper electrode in the downstream direction or letting a gap. These electrodes are connected in series to a RF, high voltage power supply. Typically, the power supply provides on the order of ten thousands of volts and at a frequency of the order of ten thousands of Hertz, suitable to maintain a plasma discharge.

A typical configuration of SDBD is shown in Figure 2.4. This type of actuator produces a flow about few meters per second when operated at 10 kV, 10 kHz. However, the performances (e.g. velocity, thrust) are strongly dependent on various parameters of the design: Dielectric thickness, dielectric properties, length of the upper and lower electrodes, length of the gap between electrodes, geometry of exposed electrode, shape function of the applied power inputs...

Effectively, these actuators act as a capacitor for low values of frequency (i.e. before the discharge occurs), with small current leakages at the operational range that correspond to the ionization of the air ([13][2]). When the upper electrode is subjected to a sinusoidal wave of voltage, an electric field develops around it, effectively developing ion species charged and electrons that move through this electrical field according to their polarity. To maintain the discharge it is needed to have a transient electric potential monotonically increasing. Therefore as a rule a DBD plasma is generated with a sinus voltage function shape.

The mechanism of thrust production is yet not fully understood. The simulation remains a difficult task, since it requires coupling Navier-Stokes equations for fluid mechanics with Poisson equation for electric field and with a kinetic model to account for the reactive aspects.

Following several authors this process of conversion of electrical power to thrust takes place in two steps: an excitation phase that ionizes the fluid (through glow discharges or streamer discharges, for negative and positive electrode polarity respectively) and a second phase where no more ionization occurs and the ions move to create a body force. In order to bypass the difficulties inherent to the simulation of the thrust resulting from a DBD, a simplified model will be used instead. This model will be explained in the following sections.

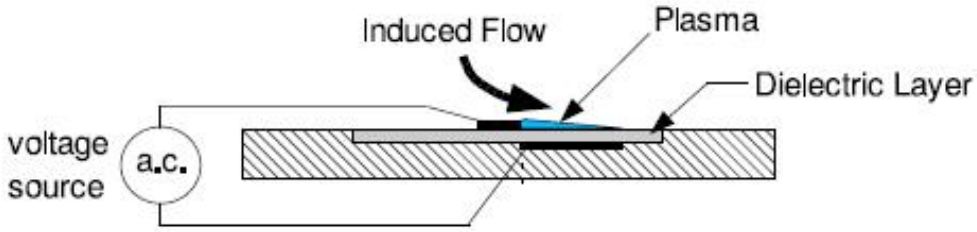

Figure 2.4: [2] Schematics of flow induced by a single DBD actuator.

2.4 Past applications

Several studies were performed in the past regarding time dependent flow control over a cylinder by means of DBD actuators. This are the most relevant:

- Alex V.Kozlov [15] performed an experimental study motivated by the need to reduce the landing gear noise for commercial transport aircraft. Special focus given to the actuator optimization and the different effect between steady and unsteady actuators. With a Re = 30000, it was found that using steady or unsteady actuation, Kármán shedding is totally eliminated, turbulence in the wake decreases significantly and a near-field sound pressure levels are reduced by 13.3 dB. Unsteady actuation at an excitation frequency of St = 1 was found to be the most effective. However, steady

actuation is more suitable for noise control applications.

- Romain Futrzynski [4] implemented the Shyy model [5] into a numerical simulation to asses the effect of active flow control on the cabin of trucks by reducing the drag produced. The model was shown to be able to accurately reproduce the wall jet created by a single plasma actuator in a no-flow condition against experimental data. Then, a half cylinder geometry, representing the A-pillar of a truck was used in a Large Eddie simulation (LES) study that showed that the actuator alone, operated continuously, was not sufficient to achieve a significant reduction of the drag. Nevertheless, a significant drag reduction was obtained by increasing the strength of the body force to higher values, showing that this type of actuation reminds relevant for drag reduction. Finally, dynamic course decomposition was investigated as a post-processing tool to improve the efficiency of the actuator.

- L. Barbato [2] performed an experimental study on the results' sensitivity to the main DBD plasma actuator parameters: thickness, lower and upper electrode width, gap length, frequency and waveform. In addition, DBD actuators were designed and installed on a cylinder and an airfoil to investigate their potentialities to reduce the flow separation occurring in low speed regime. The effect on the flow was explored by means of smoke visualization and a hot wire measurement. It was concluded that the DBD actuation can be used to control or reduce the instabilities arising from flow separation but this is limited to low Reynolds number.

  Because of interest for the present project, the result of L. Barbato are shown in Figures 2.5 and 2.6 for them to be later compared with the numerical results.

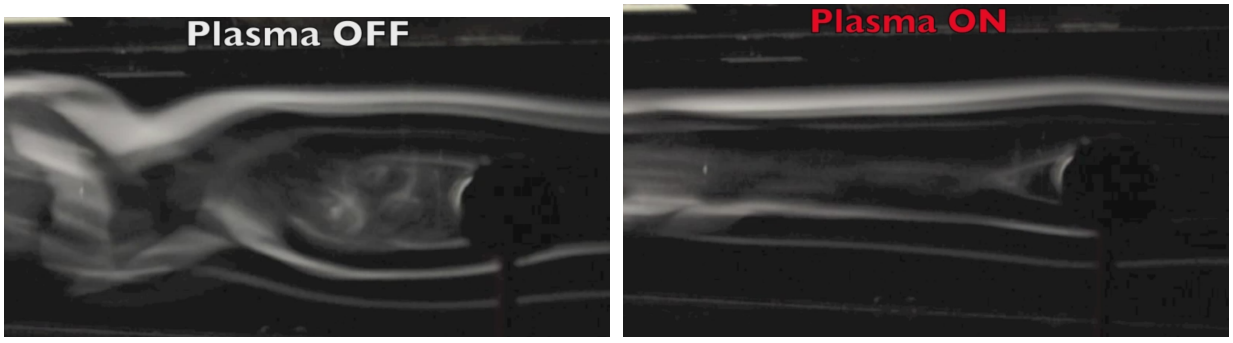

(a) Experimental flow visualization with actuators OFF (b) Experimental flow visualization with actuators ON

Figure 2.5: Experimental flow visualization

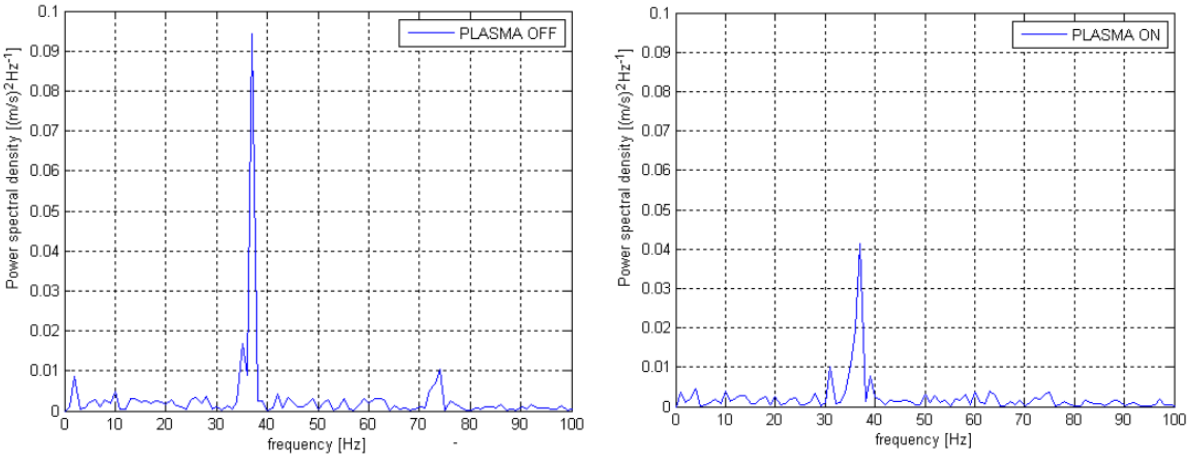

(a) Experimental FFT with actuators OFF

(b) Experimental FFT with actuators ON

Figure 2.6: Experimental FFT

Chapter 3

Numerical solver assesment

The previously mention Merged model will be exhaustively explained in the next section. This model will be implemented in a CFD solver with different geometries arranged in different configuration with the final purpose of deeply study the effect of the actuators to the Von Kármán phenomena. In this chapter, it will be explained how the different simulations were performed.

The methodology will consist on implementing the body force resulting from the Merged model to the Navier-Stokes equations. Then, the simulation will be run until convergence and results will be extracted and analyzed. The input parameters are the Navier-Stokes equations, the geometry of the problem and the model of the actuators. Then the results of the velocity profiles and drag coefficients at different positions will be extracted together with animations to capture the behavior of the Von Kármán vortices.

3.1 CFD solver

The CFD solver to be used is Fluent, included into the ANSYS Suit. This software is used for simulations of structures, fluid-dynamics and electromagnetic through finite difference method. First, the fluid is discretized in multiple cells, then the system is solved iteratively until a certain difference between the previous and the new calculation is obtained.

An implementation of the body force coming from the Merged model must be performed. To that end, Fluent provides a tool to modify different parameters of the program and the equations through User Defined Functions (UDF). UDF's are programmed in C code in a notepad with the parameters that model the fluid to be calculated enabling the user to simulate any type of behavior.

3.2 Problem parameters

3.2.1 Turbulence model

As previously mentioned, due to the range of Reynolds numbers to be used in this work, the vortex street is fully turbulent. Turbulence results in much larger skin friction, heat transfer rates and species mixing, compared to laminar flows. Hence, the implementation of a turbulence model is an inevitable portion of any Computational Fluid Dynamics (CFD) code which hopes to simulate real-world situations and obtain

realistic results at this range of Reynolds numbers.

A common view of turbulent flows is that they consist of a range of scales, with the size of the large scales determined by the geometry, and the size of the small scales determined by the fluid viscosity. The broad range of spatial and temporal scales observed in a turbulent flow make it impossible to capture the details of all those scales. Resolving the smallest scales would require very small cell spacing and time steps. This led to the idea of resolving only a certain range of scales, typically the larger ones, while modeling the effect of the smaller scales. Two of the most popular turbulence modeling approaches are Large Eddy Simulation (LES) and Reynolds-Averaged Navier Stokes (RANS) methods.

The LES method models only the smallest scales while resolving all the larger scales. Hence, in general, it is able to produce accurate results for a wide range of flow configurations. However, as the Reynolds number Re of the flow increases, the range of scales to be resolved also increases. This leads to increased computational cost when using LES models for high Re flows, which is usually the case for practical engineering configurations. The computational resources required to simulate such a flow using a LES model are prohibitive.

RANS methods on the other hand capture only the mean flow (or sometimes only the largest scales) while modeling the effect of all the fluctuations. Since a much larger portion of the scales are now being modeled, this leads to a larger error in the computed solution (in general). RANS models are usually calibrated based on attached flows such as flow over a flat plate or channel flow, and hence they work well for such cases. However, for cases involving a separation region like the flow over a cylinder studied in this project, they may be inaccurate.

The computational expense of LES and the inaccuracies of RANS for more complex flows motivated the development of hybrid RANS/LES methods. In wall bounded flows, much of the expense of LES arises due to a requirement for small cell spacing in the boundary layer. Hence the idea of using a RANS method to compute the attached boundary layer region and an LES method to compute the flow past the separation point is an attractive proposition cost-wise. Hybrid models are relatively new in the field of turbulence modeling, and have garnered the interest of many researchers.

A scheme of the turbulent models available in Fluent is depicted below, specifying the different models within the RANS method: Spalart-Allmaras, Standard k-ϵ, RNG k-ϵ, Realizable k-ϵ, Standard k-ω, SST k-ω and Reynolds Stress Model.

Detached Eddy Simulation

As previously explained, in order to reach accurate result while reducing computational cost, the selected turbulence model to perform the simulations is the so-called Detached Eddy Simulation (DES). DES is a hybrid turbulence model included in Fluent which attempts to treat near-wall regions in a RANS-like manner, and treat the rest of the flow in an LES-like manner. A turbulence length scale is obtained from the model's equations and is compared with the grid length scale to switch between

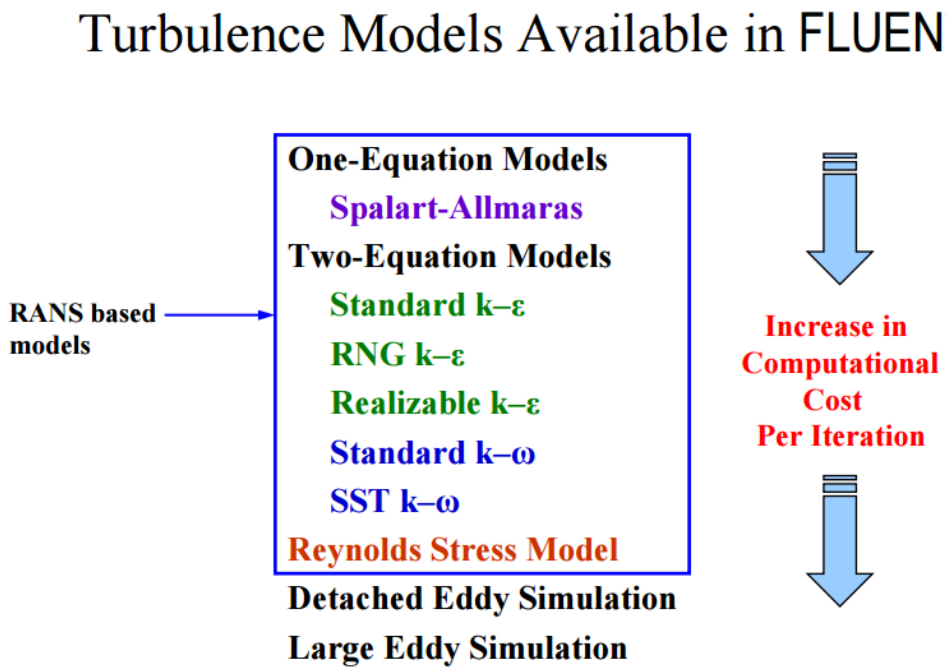

Figure 3.1: Turbulent models available in Fluent

LES and RANS. This model promise to accurately simulate the flow past a cylinder, a configuration characterized by a high degree of flow separation. In particular, the RANS and LES models selected within the DES model is works as follows:

RANS model

The RANS model selected is the two equations Menter's SST k-ϵ formulation. This model mixes the k-ϵ model transformed from the standard k-ϵ one for the outer layer of the flow and the Modified Wilcox' k-ϵ model for the inner layer.

LES model

When the Large Eddy Simulations equations are solved, the spectrum of turbulent eddies in the Navier-Stokes equations is filtered. This filter is a function of the grid size. Eddies smaller than the grid size are removed and modeled by a subgrid scale (SGS) model. Larger eddies are directly solved numerically by the filtered transient Navier-Stokes equation.

Navier-Stokes equations

$$\frac{\delta \rho}{\delta t} + \Delta \cdot (\rho \bar{U}) = 0$$

$$\frac{\delta}{\delta t}(\rho \bar{U}) + \Delta \cdot (\rho \bar{U} \bar{U}) = \Delta p + \Delta \cdot \bar{\bar{\tau}}' + \rho \vec{F}_B$$

Where ρ is the density, $\bar{U}$ is the averaged velocity, $\bar{\bar{\tau}}'$ is the viscosity tensor and $\vec{F}_B$ is the body force produced by the actuator.

The simulations considering just a flat plate with an actuator with no incoming velocity were solved using the Navier-Stokes equation, which are three, considering that the momentum equation has two components.

For the simulation solving the flow around a cylinder, the DES turbulence model equations were included, resulting in a total of five equations.

3.2.2 Boundary conditions

For cases in which only actuators placed on a flat plate was considered, inlet, outlet and upper boundary were set to be pressure-outlet. Pressure-outlet condition makes the fluid pressure to match the ambient pressure on the limiting cells without changing the velocity of the fluid. This simulates the condition of open test bench.The lower limit was set to wall condition, where there is no mass or momentum transfer from and to the boundary layer. Furthermore, the tangential velocity of the fluid is also 0 on the wall, complying with the non-slip condition.

For cases in which the flow over a cylinder was solved, the inlet section was set to be a velocity-inlet, with different velocities for each case, the outlet was set as a pressure-outlet and the cylinder, together with the upper and lower boundaries were set as walls.

3.2.3 UDF inclusion

To implement the merged model, Fluent provides a UDF tool that allows to include a body force on the equation, through a code written in C and read from a notepad. This force is applied in every cell according to the conditions specified in the code.

The inclusion is done in two steps. First, Soloviev's model term is calculated as an independent constant. Then it is multiplied by the distribution from the Singh model. The specific formulation will be explained in chapter 4.

To implement the distribution in any desired angle, a rotation of the actuator must be performed. Fluent takes by default as imputs parameters of the UDF the position relative to the global coordinate system of the center of the cell to be calculated. The rotation with an angle α is:

$$\vec{x}' = x_0 + (\vec{x} - x_0) \cdot cos(\alpha) - (\vec{y} - y_0) \cdot sin(\alpha)$$

$$\vec{y}' = y_0 + (\vec{x} - x_0) \cdot sin(\alpha) - (\vec{y} - y_0) \cdot cos(\alpha)$$

Where x_0 is the horizontal position of the actuator and y_0 is the vertical dielectric thickness. α is defined positive clockwise. These parameters are then evaluated in the Merged model, obtaining the force applied in the local coordinates.

This force is retrieved by the UDF in the global coordinate system as well, so a conversion of the force back to that coordinate system must be performed as well. This is given by:

$$\vec{F_x} = \vec{F_x}' \cdot cos(\alpha) + \vec{F_y}' \cdot sin(\alpha)$$

$$\vec{F_y} = -\vec{F_x}' \cdot sin(\alpha) + \vec{F_y}' \cdot cos(\alpha)$$

The Figures 3.2 and 3.3 show the velocity distribution of an actuator placed in a flat plate in normal configuration and rotated 45 degrees. Note that the result was obtained by creating a new domain and including in the code the above-mentioned formulation.

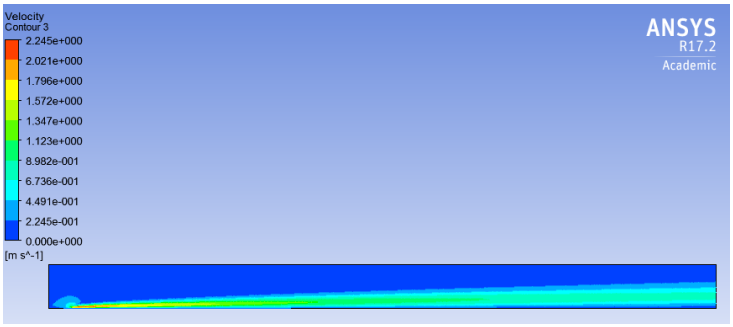

Figure 3.2: Simulation of a single actuator using the Merged model

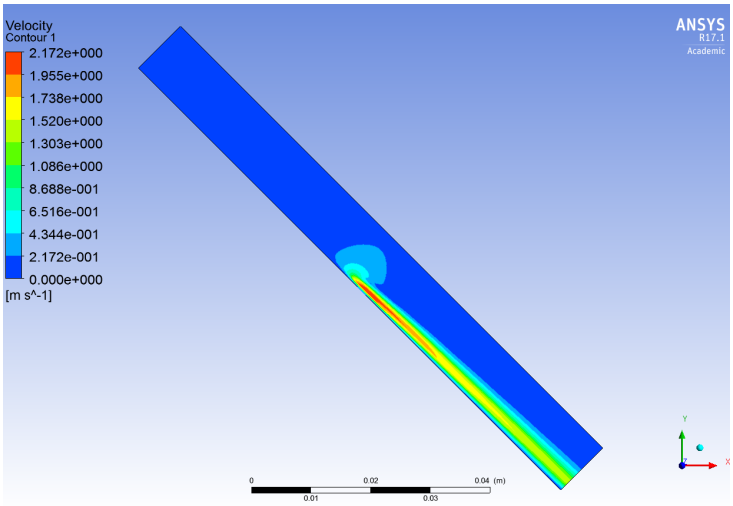

Figure 3.3: Simulation of a single actuator rotated 45 degrees using the Merged model

3.2.4 Convergence criteria

To consider the simulation converged, the criteria used was the convergence of the residuals. These are the difference in the Navier-Stokes equations from a computational step to the next one. When this difference is small, the fluid is considered to be converged. In the case of a time dependant computation, this process is repeated for every time step.

This residuals were set to 10^{-6} for the continuity and momentum equations in steady calculations. In the case of transient cases, the residual has been set to 10^{-3} for the continuity equations and 10^{-5} for the momentum and turbulent equations.

The following chart shows how the different parameters mentioned in this chapter interact with each other in the Fluent solver in order to reach a solution.

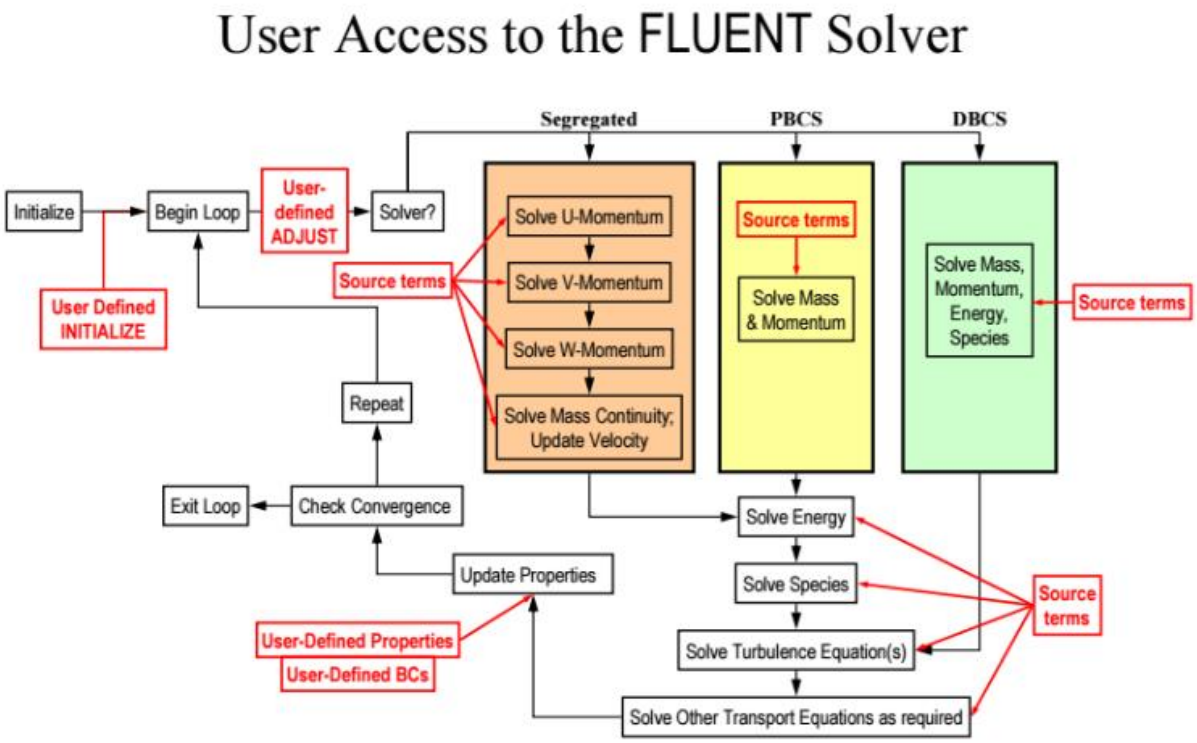

Figure 3.4: Fluent workflow

Chapter 4

Model sensitivity

4.1 Model fundamentals

Soloviev's model

The aim of Soloviev was to estimate analytically the force produced by a SDBD by means of a phenomenological model with experimental data and applying plasma physics theory, in order to define a simple analytic expression well suited for coupling with Navier-Stokes equation. From his work, we know the following expression:

$$F_{sol} \approx 2.4 \times 10^{-10} \alpha_l^4 \frac{f_V(kHz)}{d(cm)} \left(\frac{9V_0}{4\Delta V_c}\right)^4 \left(1 - \frac{7\Delta V_c}{6V_0}\right)^4 \left(1 - exp\left(-\frac{1}{4 f_V \Delta\tau_q}\right)\right)$$

Where f_V denotes the frequency applied, d is the thickness of the dielectric, V_0 the applied voltage peak-to-peak, ΔV_c the normal falldown of cathode voltage, α_l a fitting parameter, usually set to unity; and $\Delta\tau_q$ is the residence time of negative ions inside the acceleration volume.

This model is only able to give a global thrust, and does not give any insight on the distribution of said thrust.

Singh model

The aim of the investigation reported in Singh was to produce a satisfying description of the distribution of the body forces produced by a SDBD. this work was based on previous exact computations (solving Navier-Sotkes, Poisson and kinetic equations for several species), and a relationship between EHD force and problem parameters has been approximated.

The resulting expression is as follows:

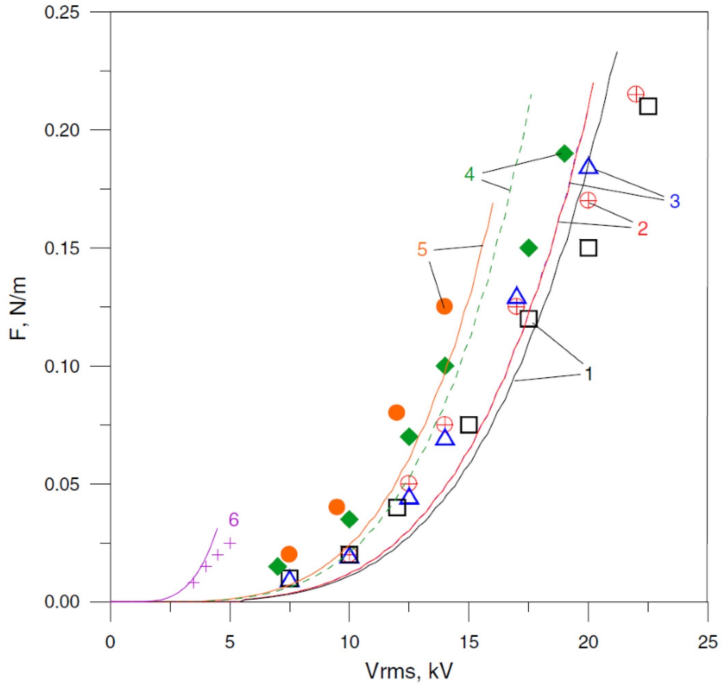

Figure 4.1: [8] Theoretical estimation of the Soloviev thrust per unit electrode length (lines) against experimental data (symbols) for 1—Teflon (ε = 2), d = 6.35mm, fv = 2.1kHz; 2—Derlin (ε = 3.5), d = 6.35mm, fv = 2.3kHz; 3—quartz (ε = 4.2), d = 6.35mm, fv = 2.3kHz; 4—Teflon(ε = 2), d = 3.18mm, fv = 2kHz; 5—Macor (ε = 6), d = 3.18 mm, fv = 2.3 kHz; 6—Kapton (ε=3.9),d=0.15mm,fv =4.4kHz; $Vrms = V0/1.7$.

$$\vec{F}(x,y) = F_{x0}\phi_0^4 exp\left[-\left(\frac{x - x_0 - (y - y_o)}{y}\right)^2 - \beta_x(y - y_0)^2\right]\hat{i}$$
$$+F_{y0}\phi_0^4 exp\left[-\left(\frac{x - x_o}{y}\right)^2 - \beta_y(y - y_0)^2\right]\hat{j}$$

Where x_0 is the horizontal position of the actuator and y_0 is the dielectric thickness. F_{x0}, F_{y0} are average thrust parameter obtained from the numerical solution of air-plasma equations, ϕ_0 is the applied voltage and β_x and β_y are function of the dielectric material.

However, this model is not reliable in terms of global thrust, but reliable in the force distribution.

Merged model

None of this two models is able to describe the EHD distribution, as Soloviev's model provides the global force without the distribution and Singh model predicts the distribution but fails to give the global thrust.

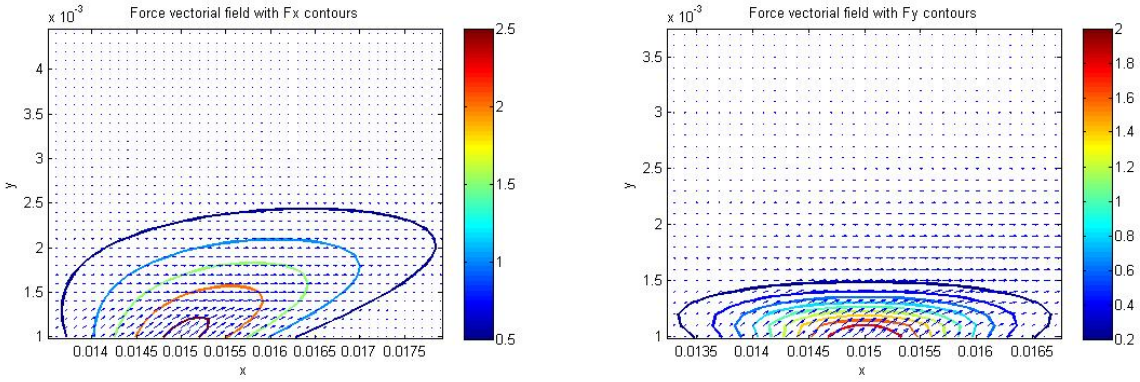

(a) (b)

Figure 4.2: Singh vectorial force distribution with F_x and F_y contours respectively.

For this reason L. del Amo [1] decided to merged both models. The approach followed was to normalize the Singh equation and multiply the result by the Soloviev force to finally obtain a value which predicts both the global force and the distribution of forces provided by the actuator.

the methodology followed was to integrate the force imparted by the model along the simulation volume. The limits of integration were considered to be at infinity, although practically a finite volume has to be set. This was done in increasing steps until a steady value of the results was obtained for each component. The integral to be performed is:

$$\vec{F} = \int\int F_{x0}\phi_0^4 exp\left[-\left(\frac{x - x_0 - (y - y_o)}{y}\right)^2 - \beta_x(y - y_0)^2\right]\hat{i}$$
$$+F_{y0}\phi_0^4 exp\left[-\left(\frac{x - x_o}{y}\right)^2 - \beta_y(y - y_0)^2\right]\hat{j}dxdy$$

Parameter ϕ_0 was set to unity for the distribution not to be dependent on the voltage, as this parameter will come from Soloviev's term. The rest of the parameter are set following recommendations specified in the Singh work: $F_{x0} = 2.6$, $F_{y0} = 2$, $x_0 = 0.005$, $y_0 = 0.001$, $\beta_x = 8 \times 10^5$ and $\beta_y = 10^7$.

Following L. del Amo's work, the normalization is performed by obtaining an expression that fulfills:

$$\frac{\int\int \vec{F}(x, y)dxdy}{K} = 1$$

According to this expression, K is equal to the modulus of the force resultant from the integral. For the case in which the avobe mentioned constants are used, $K = \|\vec{F}\| = 7.5375 \times 10^{-6}$.

The normalized force is obtained as follows:

$$\vec{f}(x,y)_{normalized} = \frac{\vec{F}(F_{x0}, F_{y0}, \beta_x, \beta_y)}{\|\vec{F}\|}$$

Therefore, the final expression is obtained by multiplying this normalized force to the Soloviev's force, obtaining:

$$\vec{T_0} = F_{sol}(d, V_0, f_V) \cdot \frac{\vec{F}(F_{x0}, F_{y0}, \beta_x, \beta_y)}{\|\vec{F}\|}$$

It is of huge importance to remind that y_0 is not the vertical position of the actuator, but the dielectric thickness and it is a constant, $y0 = 0.001$. In order to apply this model to different positions and rotation angles the previous formula has to be slightly modify by introducing a value y_{ref} which does account for the vertical position. This value together with x_0 will place the model wherever wanted. Therefore, the ultimate expression is:

$$\vec{T_0} = 2.4 \times 10^{-10} \alpha_l^4 \frac{f_V(kHz)}{d(cm)} \left(\frac{9V_0}{4\Delta V_c}\right)^4 \left(1 - \frac{7\Delta V_c}{6V_0}\right)^4 \left(1 - exp\left(-\frac{1}{4 f_V \delta \tau_q}\right)\right) \cdot \frac{1}{\|\vec{F}\|} \cdot$$
$$\left[F_{x0}\phi_0^4 exp\left[-\left(\frac{x - x_0 - (y - y_{ref} - y_0)}{y}\right)^2 - \beta_x (y - y_{ref} - y_0)^2\right]\hat{i}\right.$$
$$\left. + F_{y0}\phi_0^4 exp\left[-\left(\frac{x - x_0}{y}\right)^2 - \beta_y (y - y_{ref} - y_0)^2\right]\hat{j}\right]$$

The resulting DBD actuator force distribution is explicitly dependent on various parameters, related to the configuration (dielectric thickness) of the DBD and the operating settings (frequency and voltage)

Moreover, this model includes also dependencies to specific parameters that depend implicitly on the arrangement setting. This parameters are constants which values are set based on the authors recommendations for the specific models. This values, which will be used for the rest of the work, are defined in Table 4.1.

α_l	ΔV_c	F_{x0}	F_{y0}	β_x	β_y	$\|\vec{F}\|$
1	$600V$	2.6	2	$8 \cdot 10^5$	10^7	$7.5359 \cdot 10^{-6}$

Table 4.1: Parameters' values in nominal situation

4.2 β_x and β_y model sensitivity

As previously mentioned, the Merged model depends on several parameters that are implicitly related to arrangement settings. This arrangement settings may be the shape of the electrode, its material or the voltage features, among others. Following the authors recommendations, the above mentioned constants are

used to perform nominal configuration simulation. Nevertheless, it is of interest to know the dependence of the result to this parameters in order to fit the model to the reality for non-nominal configuration.

This dependence can be assessed comparing the difference in the force distribution and induced velocity profile when changing the parameters of a single actuator placed in a flat plate simulated in steady conditions.

Different values of β_x and β_y were introduced in the Merged model to analyze and compare the results. The following nominal values were set as reference of the study: $\beta_x = 8 \cdot 10^5$ and $\beta_y = 10^7$. Then each of them was multiplied and divided by 10 keeping the other one unchanged. Note that for every set of β_x and β_y values a different $\|\vec{F}\|$ value has to be calculated. This is due to the fact that the parameters change the Singh force distribution that in normalized and consequently the value of the integral changes. $\|\vec{F}\|$ was calculated following the methodology explained in previous section selecting the appropriate limits of integration at each case.

The following values were used:

β_x	β_y	F_x	F_y	$\|\vec{F}\|$
β_{x0}	β_{y0}	7.4460×10^{-6}	1.1707×10^{-6}	7.5375×10^{-6}
$10 \cdot \beta_{x0}$	β_{y0}	1.73196×10^{-6}	1.1707×10^{-6}	2.0905×10^{-6}
$\beta_{x0}/10$	β_{y0}	43.1029×10^{-6}	1.1707×10^{-6}	43.1187×10^{-6}
β_{x0}	$10 \cdot \beta_{y0}$	7.4460×10^{-6}	0.33188×10^{-6}	7.4534×10^{-6}
β_{x0}	$\beta_{y0}/10$	7.4460×10^{-6}	4.9115×10^{-6}	8.9101×10^{-6}

Table 4.2: β_x, β_y and integrated force values

Once the simulation is converged, V_x profile along the y axis and V_y profile along the x axis in three different points each is extracted. V_x profile is calculated in the vertical lines at 1, 3 and 5 cm away in the horizontal direction from the actuator. V_y profile is calculated in the horizontal lines at 0.25, 0.5 and 0.75 mm away in the vertical direction from the actuator.

Figures 4.4 and 4.3 show how the force distribution varies with β_x and β_y. An increase in β_x makes the distribution to contract and the global value of the force to be more concentrated. As seen in Figure 4.5, this makes the V_x profile to be thinner and with higher values but with less momentum as the velocity values rapidly decrease when moving along the x axis. In the other hand, a decrease in β_x makes the distribution to elongate and the global value of the force gets diluted. This makes the V_x profile to be thicker and with lower values but with more momentum as the velocity values barely decrease when moving along the x axis.

Increasing β_x makes the total y component of the force to be even smaller. The force distribution of this model is characterized by the fact that F_x is much larger than F_y. For this reason, increasing β_x, the flow reminds almost unchanged. In the other hand, when β_y is reduced, the y component of the force increases in such a way that the x component is not dominant anymore. This makes the total value of

the integral explained in section 4.1 to be increased, as F_x reminds unchanged and F_y increases. This explains the reduction of the values in the V_X profile.

The V_y presents much lower values than V_x and it has very small changes when varying β_x and β_y. The only relevant effect is the suction peak created ahead the actuator due to mass conservation when varying β_x. Increasing β_x, the values on V_x increases close to the actuator and consequently the suction peak increases. Conversely, decreasing β_x, the values on V_x decreases and consequently the suction peak decreases.

4.3 F_{x0} and F_{y0} model sensitivity

Similarly to the previous subsection, a sensitivity study of F_{x0} and F_{y0} is obtained. The nominal values are $F_{x0}' = 2.6$ and $F_{y0}' = 2$. As seen in the final equation of the merged model, F_{x0} and F_{y0} are present in the numerator and in the denominator (inside $\|\vec{F}\|$). By a simple process of factorization, it is found that the model is not sensitive to independent values of F_{x0} and F_{y0}, but to the ratio of these two, $r = \frac{F_{x0}}{F_{y0}}$.

Different values of r were obtained by multiplying F_{x0} by 2 and 20 keeping F_{y0} unchanged. This two provides the limiting values of r in realistic situations.The following values were used:

F_{x0}	F_{y0}	F_x	F_y	$\|\vec{F}\|$
F_{x0}'	F_{y0}'	7.4460×10^{-6}	1.1707×10^{-6}	7.5375×10^{-6}
$2 \cdot F_{x0}'$	F_{y0}'	14.893×10^{-6}	1.1707×10^{-6}	14.938×10^{-6}
$20 \cdot F_{x0}'$	F_{y0}'	148.92×10^{-6}	1.1707×10^{-6}	148.92×10^{-6}

Table 4.3: F_{x0}, F_{y0} and integrated force values

As seen in figure 4.6, only results calculated at the furthest points from the actuator are shown, as the other ones do not contribute with any additional information. Even selecting the limiting values of r, the velocity profiles have no relevant changes. This is due to the normalization process. This realistic values of r are obtained by multiplying F_{x0} by 2 to 20, meaning that the predominance of F_x over F_y is further increased. When increasing F_{x0} both numerator and denominator of the Merged model distribution increases almost proportionally as the value F_y is smaller, keeping the total value of the distribution almost unchanged. For this reason, the induced velocity profiles has negligible differences.

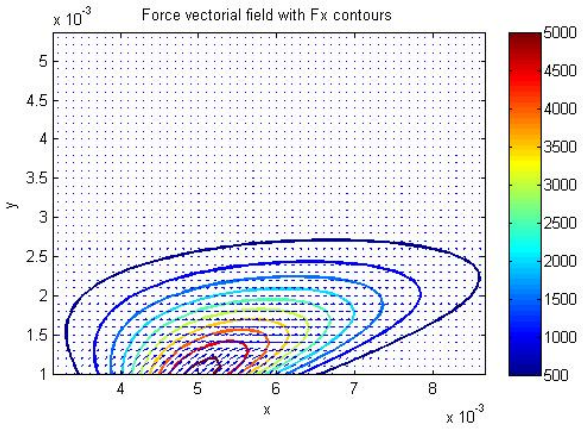

(a) F_x force contours with β_{x0} and β_{y0}

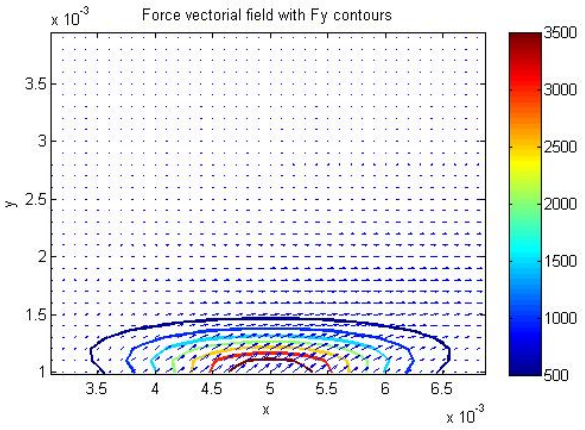

(b) F_y force contours with β_{x0} and β_{y0}

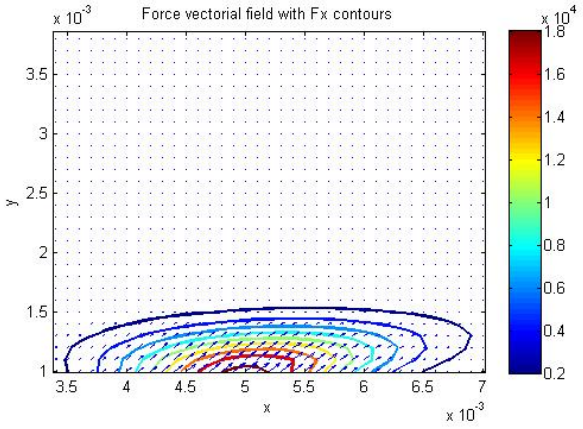

(c) F_x force contours with $10 \times \beta_{x0}$ and β_{y0}

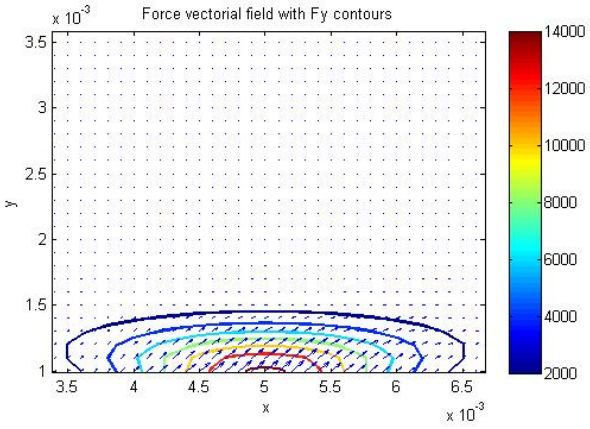

(d) F_y force contours with $10 \times \beta_{x0}$ and β_{y0}

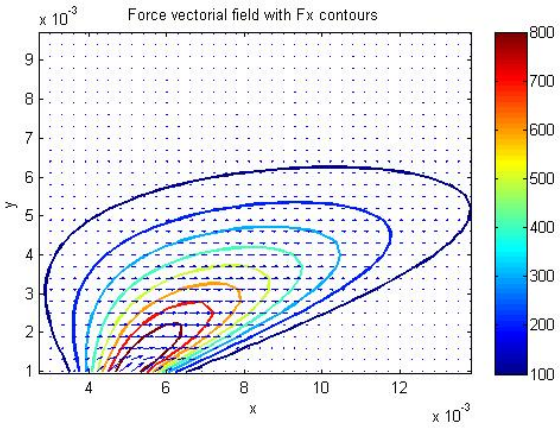

(e) F_x force contours with $\beta_{x0}/10$ and β_{y0}

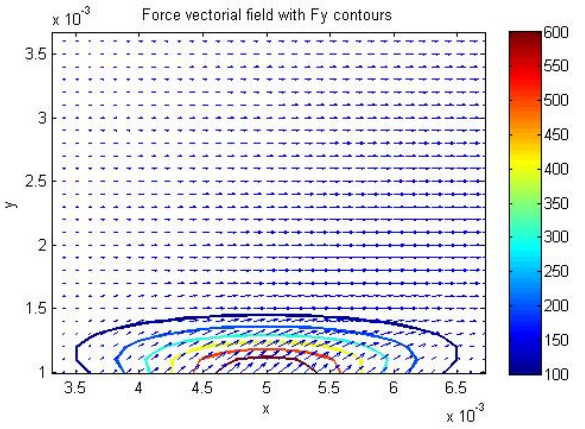

(f) F_y force contours with $\beta_{x0}/10$ and β_{y0}

Figure 4.3: Force contours for nominal case and varied values of β_{x0}

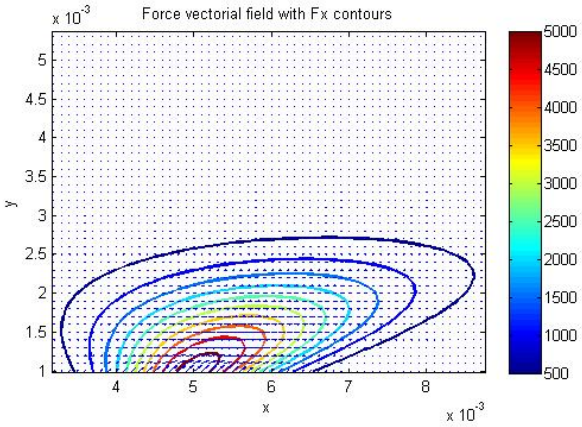

(a) F_x force contours with β_{x0} and $10 \times \beta_{y0}$

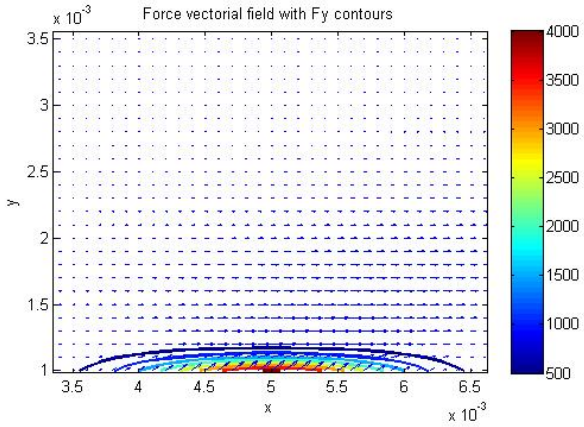

(b) F_y force contours with β_{x0} and $10 \times \beta_{y0}$

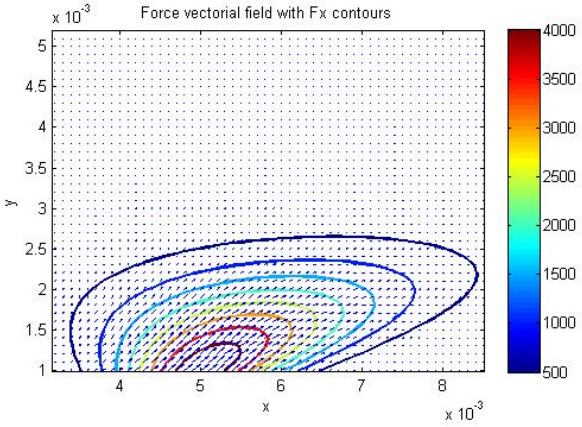

(c) F_x force contours with β_{x0} and $\beta_{y0}/10$

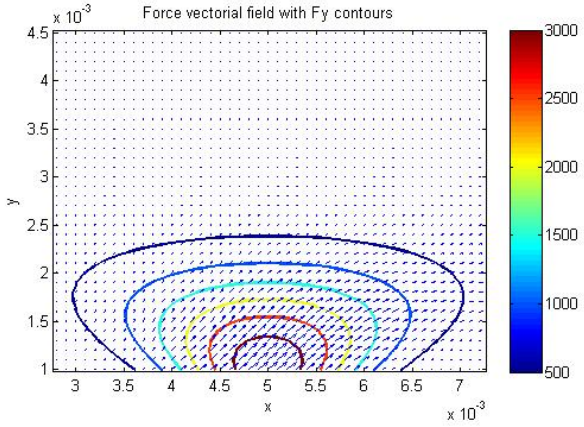

(d) F_y force contours with β_{x0} and $\beta_{y0}/10$

Figure 4.4: Force contours for varied values of β_{y0}

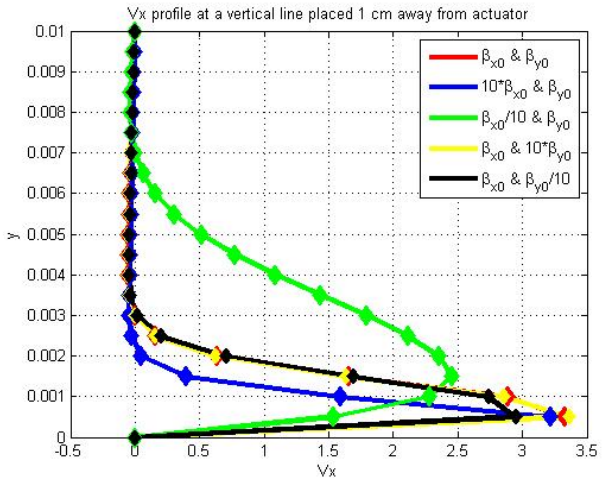

(a) Vx profile 1 cm away from actuator with different β_{x0} and β_{y0}

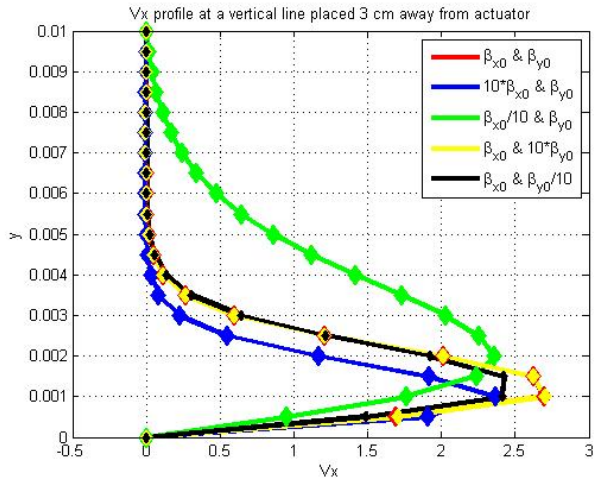

(b) Vx profile 3 cm away from actuator with different β_{x0} and β_{y0}

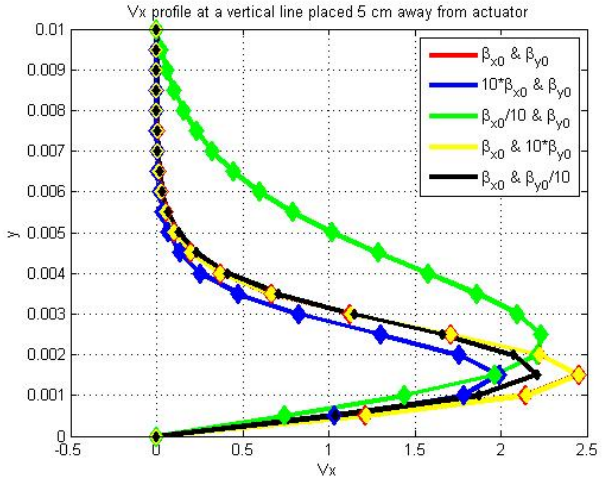

(c) Vx profile 5 cm away from actuator with different β_{x0} and β_{y0}

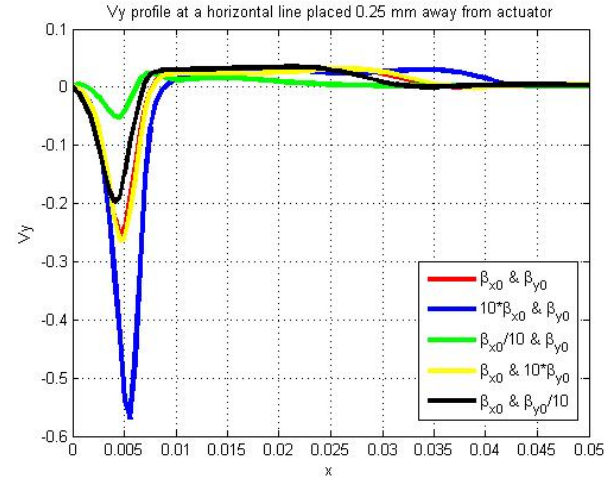

(d) Vy profile 0.025 cm away from actuator with different β_{x0} and β_{y0}

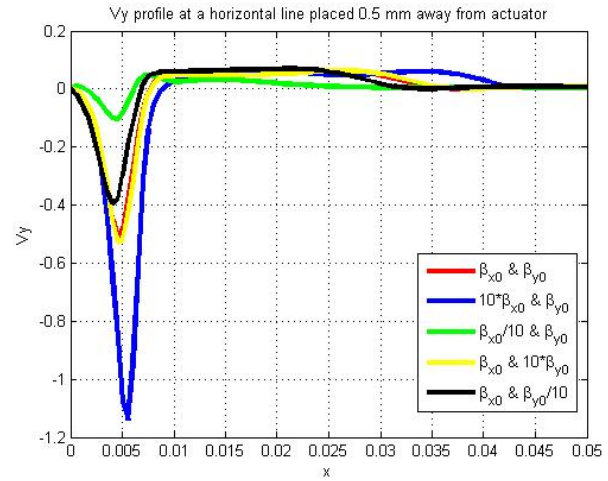

(e) Vy profile 0.05 cm away from actuator with different β_{x0} and β_{y0}

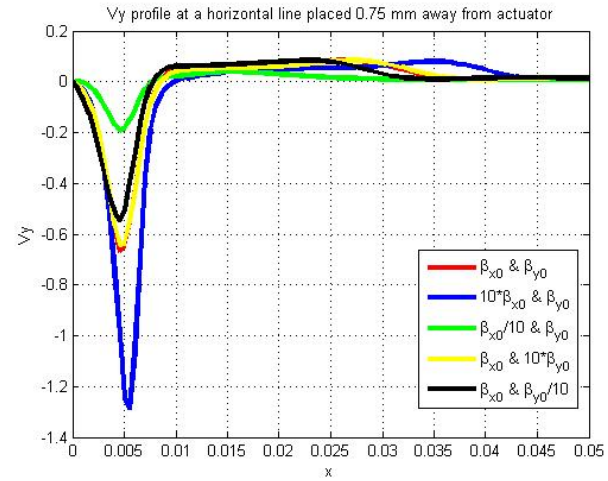

(f) Vy profile 0.075 cm away from actuator with different β_{x0} and β_{y0}

Figure 4.5: Vx and Vy profiles at different positions and β_{x0} and β_{y0} values

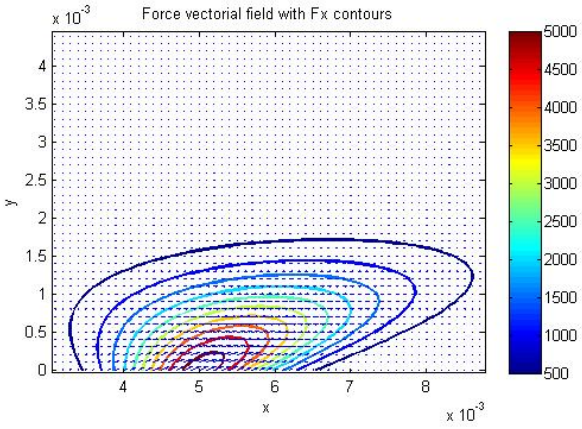

(a) F_x force contours with $2 \cdot F_{x0}'$ and F_{y0}'

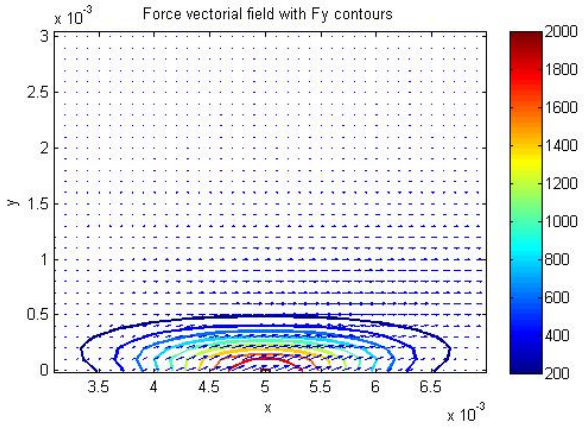

(b) F_y force contours with $2 \cdot F_{x0}'$ and F_{y0}'

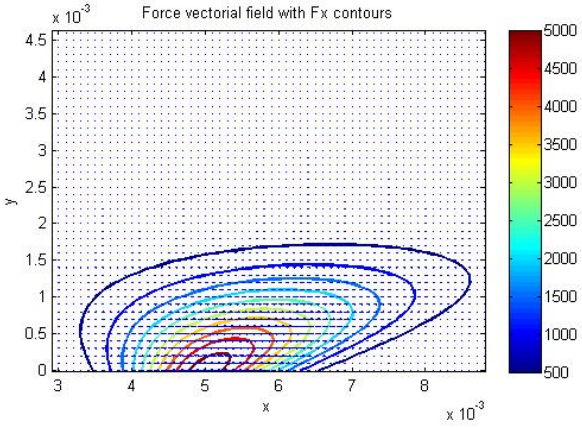

(c) F_x force contours with $10 \cdot F_{x0}'$ and F_{y0}'

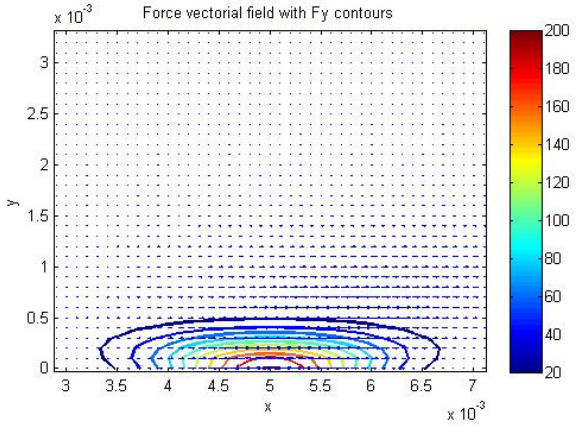

(d) F_x force contours with $10 \cdot F_{x0}'$ and F_{y0}'

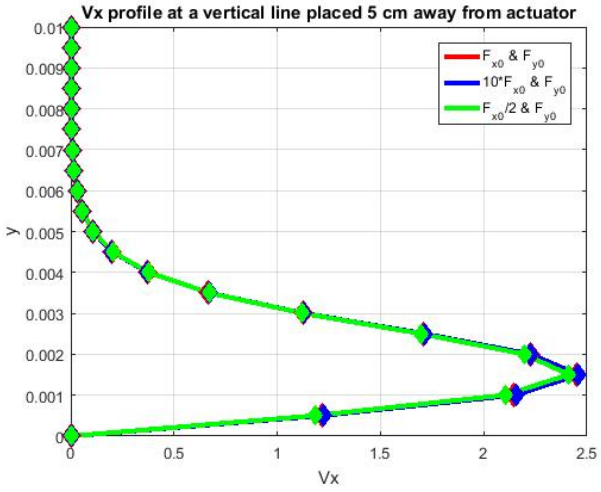

(e) V_x profile with different values of F_{x0} and F_{y0}

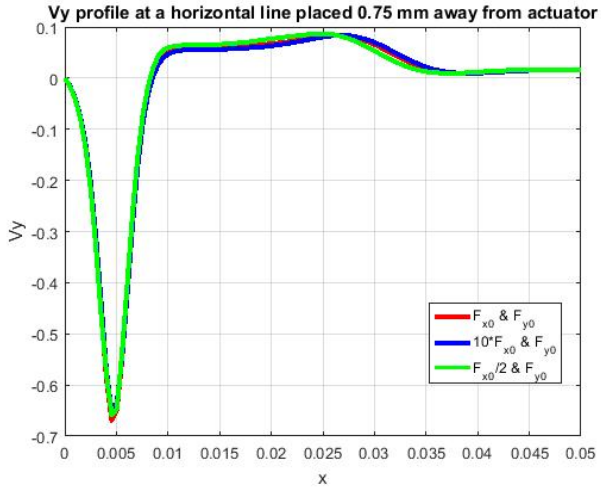

(f) V_y profile with different values of F_{x0} and F_{y0}

Figure 4.6: Force contours and V_x and V_y profiles for nominal case and varied values of F_{x0}

Chapter 5

Application to the cylinder

5.1 Problem configuration

Along this section, the problem configuration to be followed by the hole chapter will be described. In the origin of the domain, it is placed the cylinder of radius $r = 1$ cm. It is fixed and exposed to an incoming flow with velocity V that will vary depending on the simulation. The actuators will be placed by pairs and keeping symmetry with respect to the horizontal axis. The point of application of the forces will be defined by the angle θ that goes from a value of zero when placed on the y axis and increases in anti-clockwise direction. In each case, the forces are rotated in such a way that they are tangent to the cylinder surface. This configuration is sketched in 5.1.

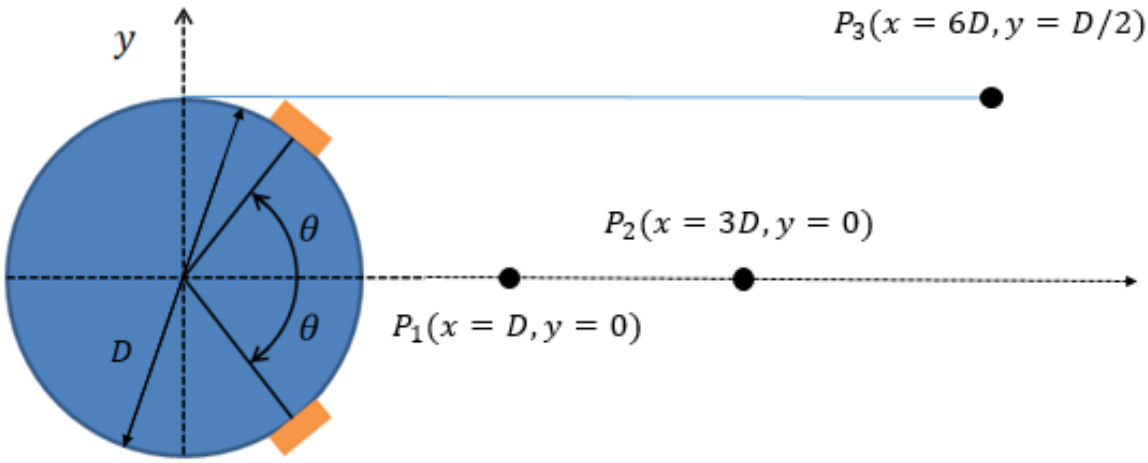

Figure 5.1: Configuration sketch (not on scale)

In a configuration such as this one over the cylinder, there exist a relation between the application point and the angle of rotation. When the actuators are placed at $\theta = \pm 90^{\text{o}}$ (at the upper and lower parts of the cylinder) the actuators are not rotated. They progressively rotate until the maximum rotation of $\alpha = 90^{\text{o}}$ is reached when $\theta = \pm 0$. For this reason, the the relation of this two angles is: $\alpha = \theta - 90^{\text{o}}$.

This way, both actuators are always tangent to the point of application.

In addition, as θ goes from 180 to 0, the resulting rotation in order to meet the desired configuration has to be in the clockwise direction. Following the formulation introduced in chapter 3, which introduces a rotation in the clockwise direction when the angle is positive, α has to be multiplied by -1 in order to make it positive.

Moreover, some parameters have to be adapted in order to perform the proper inclusion of the actuator placed at the lower part of the cylinder. More specifically, to implement the symmetry over the x axis, the y coordinate and the y component of the force have to be multiplied by -1.

Everything above-mentioned, together with the introduction of y_{ref} described in chapter 4, leads to an adaptation of the rotation formulation described in chapter 3 (which provides the most generic form).The formulation used for this application is as follows:

$$\vec{x}' = x_0 + (\vec{x} - x_0) \cdot cos(-\alpha) - (\pm\vec{y} - y_0 - y_{ref}) \cdot sin(-\alpha)$$
$$\vec{y}' = y_0 + (\vec{x} - x_0) \cdot sin(-\alpha) - (\pm\vec{y} - y_0 - y_{ref}) \cdot cos(-\alpha)$$

$$\vec{F_x} = \vec{F_x}' \cdot cos(-\alpha) \pm \vec{F_y}' \cdot sin(-\alpha)$$
$$\vec{F_y} = \vec{F_x}' \cdot sin(-\alpha) \mp \vec{F_y}' \cdot cos(-\alpha)$$

Note tha the $\pm$ signs accounts for the upper and lower actuators respectively. Figures 5.2 shows the force distribution when applying two actuators over the cylinder placed at 70º. Then, 5.3 shows the velocity contours produced by this distribution once implemented in Fluent with a symbolic incoming free-stream velocity of $0.1m/s$ to clearly distinguish the actuator effect.

5.2 Velocity limitation for flow control

In this section, two different actuators will be considered, each of them with different Soloviev's constant: the first one will have a value of $F = 0.015N/m$ and the second one exactly the double, $F = 0.03N/m$. They will be placed following the above-mentioned configuration. An angle of application of 70º will be considered. Then the free-stream velocity will be periodically increased in both cases to assess the influence of the velocity on the actuator performance. Eventually, the maximum velocity for which the actuators have a meaningful effect on the flow will be found.

The way to assess the performance of the actuator will be through the introduction of a parameter Δ. This will be the absolute value of the percentile decrease of the drag coefficient when the actuators are

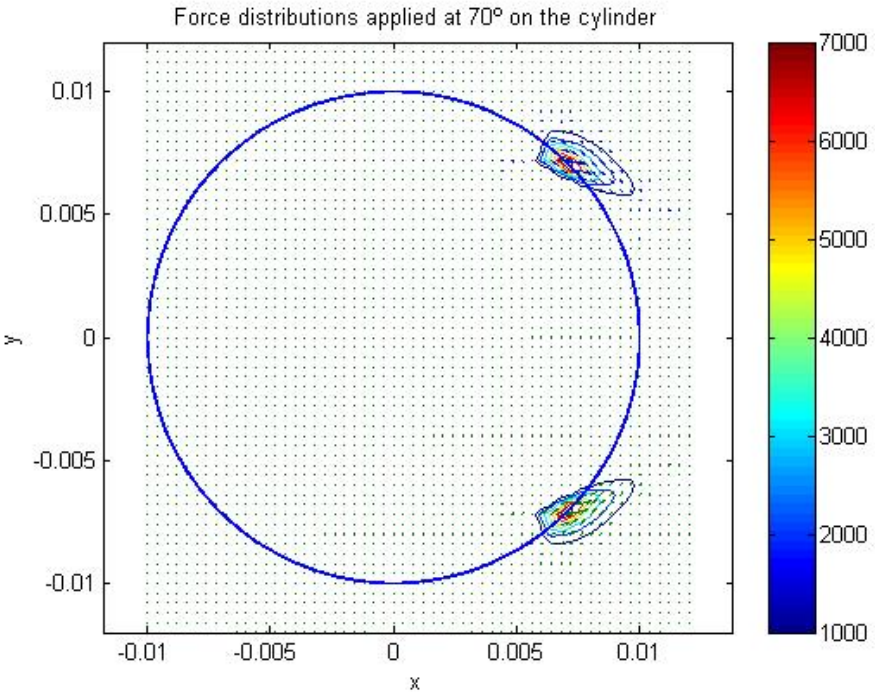

Figure 5.2: Matlab representation of the force distributions applied at 70^{o} on the cylinder

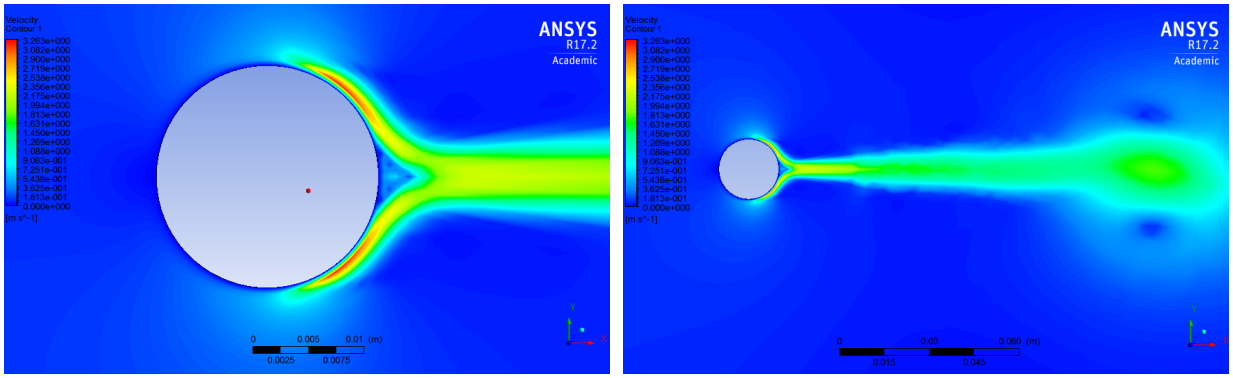

(a) Velocity contours zoom

(b) Velocity contours

Figure 5.3: Velocity contours resulted from two actuators placed at 70^{o}.

switched on with respect to when they are switched off for each incoming velocity. The drag coefficient is measured for both situations during a simulation long enough to obtain periodically stable results and then the final value is obtained by taking the average. Moreover, the limiting velocity will be considered to be that one that makes Δ to be less than 3 %. The expression is as follows:

$$\Delta = \frac{\bar{C}_{DON} - \bar{C}_{DOFF}}{\bar{C}_{DOFF}} \times 100$$

As seen in Figure 5.4 the influence of this kind of actuators is very high for a free-stream velocity of $2.5m/s$. The percentile reduction is around 80 % which means that the drag coefficient is almost reduced to zero when the actuators are on. In the other hand, when the free-stream velocity reaches 15 and 20

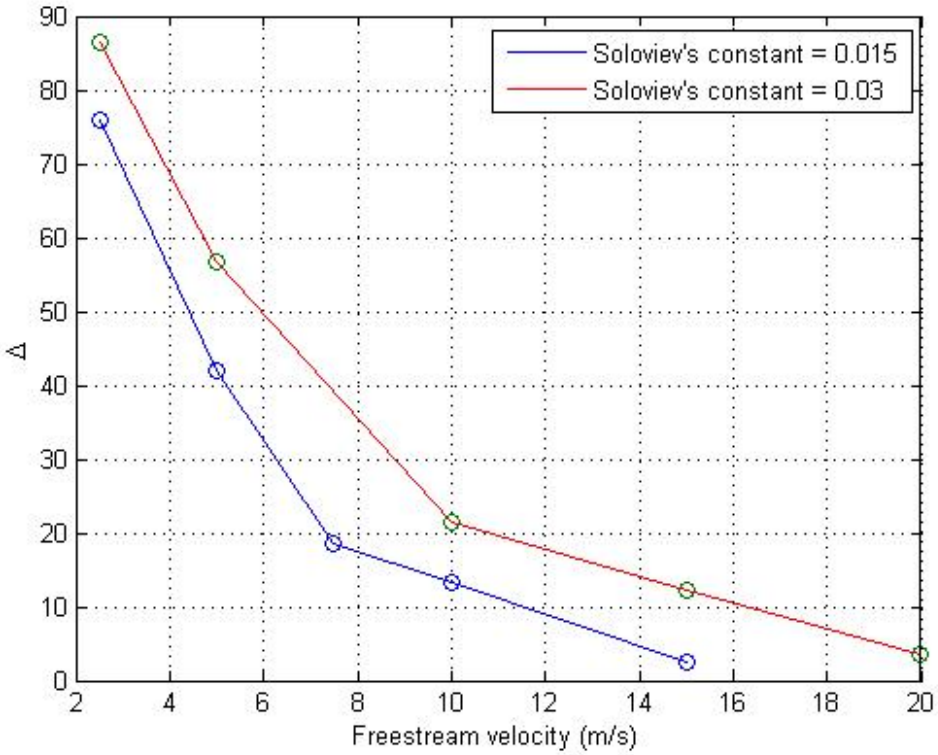

Figure 5.4: Δ versus free stream velocity

m/s respectively, the actuators does not have any meaningful effect on the flow.

This conclusions based on the value of Δ are consistent with the results. It can be visually inspected in Figure 5.5, the effect on the flow behaviour in each case. Note that only the case of Soloviev's constant $F = 0.03N/m$ is shown as the effect is more exaggerated.

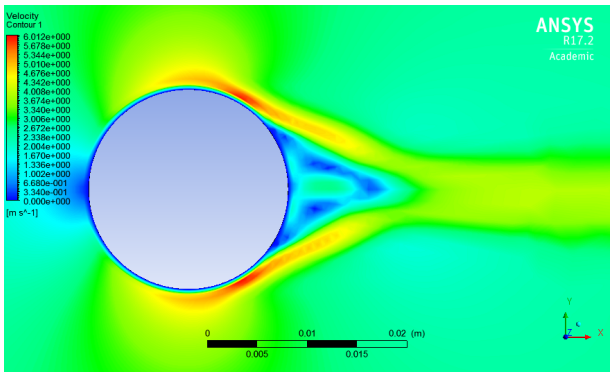

(a) $V_\infty = 2.5m/s$, actuators ON

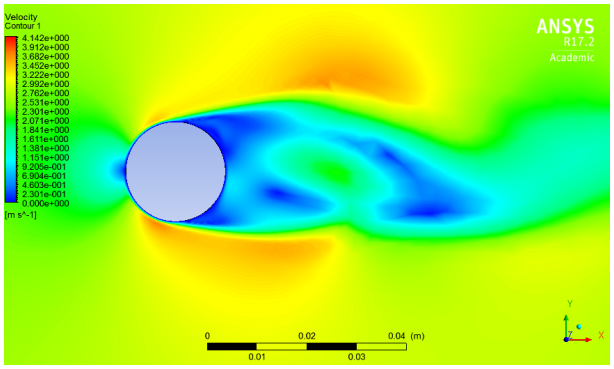

(b) $V_\infty = 2.5m/s$, actuators OFF

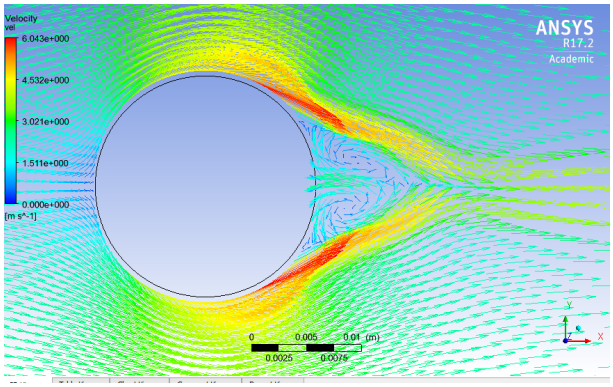

(c) $V = 2.5m/s$, actuators ON

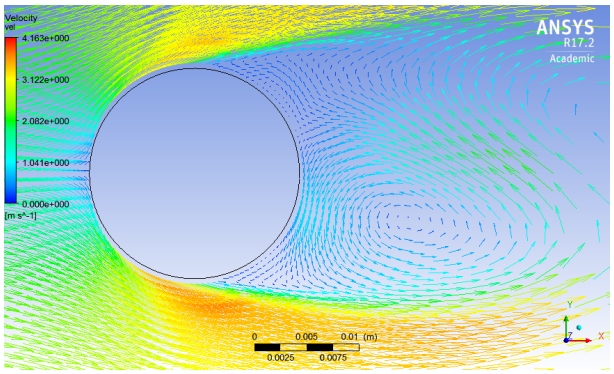

(d) $V_\infty = 2.5m/s$, actuators OFF

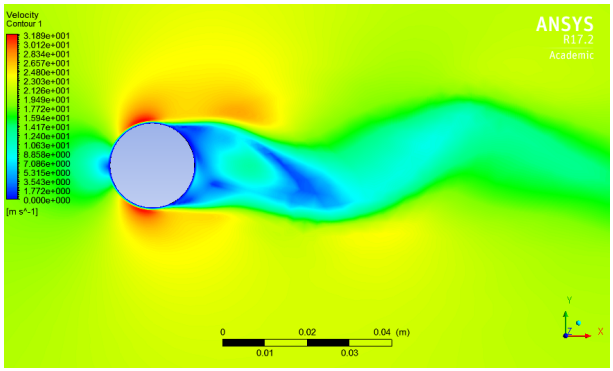

(e) $V = 20m/s$, actuators ON

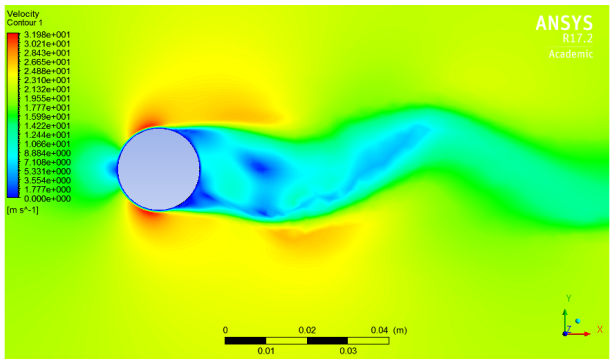

(f) $V_\infty = 20m/s$, actuators OFF

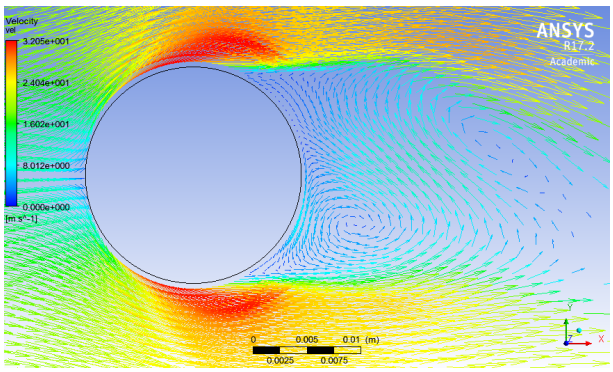

(g) $V_\infty = 20m/s$, actuators ON

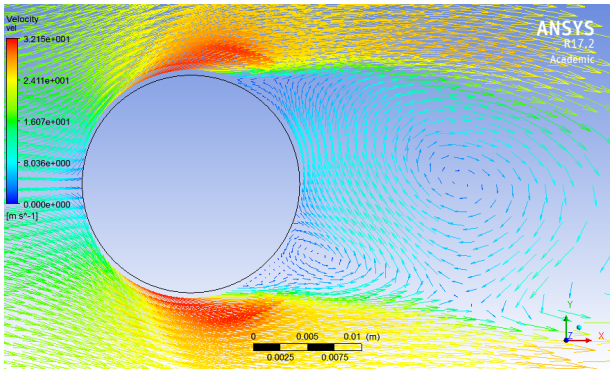

(h) $V_\infty = 20m/s$, actuators OFF

Figure 5.5: Velocity vectorial representation for different V_∞ with actuators ON and OFF

5.3 Optimal angle of actuator application

The objective of this section is to find the optimal angle of application of the actuators. In other words, the angle at which the drag reduction is maximum with respect to the case with no actuators.

To that end, a specific situation from them of the previous section was selected: Soloviev's constant $F = 0.015N/m$ and incoming velocity $V_\infty = 5m/s$. This configuration has been selected as the results from previous section suggest that it will give significant difference in the results that enables to reach meaningful conclusions. Keeping the force and velocity as constants, the angle was varied from 0 to 180 degrees in order to find the most efficient position.

Figure 5.6 shows the results of this study. It can be seen that the optimal angle is $\theta = 82.5^{\text{o}}$. At this angle, the boundary layer has not been detached yet, and the hole force distribution from the actuator contributes for it to remain attached. If the angle is further decreased from that value, Δ also does. Then a region, between 70 and 55 degrees can be differentiated. In this region, the force from the actuator is partially contributing for the flow to remain attached to the cylinder. For this reason, Δ decreases but still has a reasonable value. This happens until a sudden drop is encountered. This drop is due to the fact that the distance from the flow separation point and the position of the actuator is sufficiently high for a re-circulation bubble to be developed. This phenomena holds from 50 degrees on.

Surprisingly, if the actuators are placed in the exposed region of the cylinder, this is, from 90 degrees on, the actuation effect is still positive. Not only that, but in this region of application, Δ is even higher that the one corresponding to the region dominated by the re-circulation bubble.

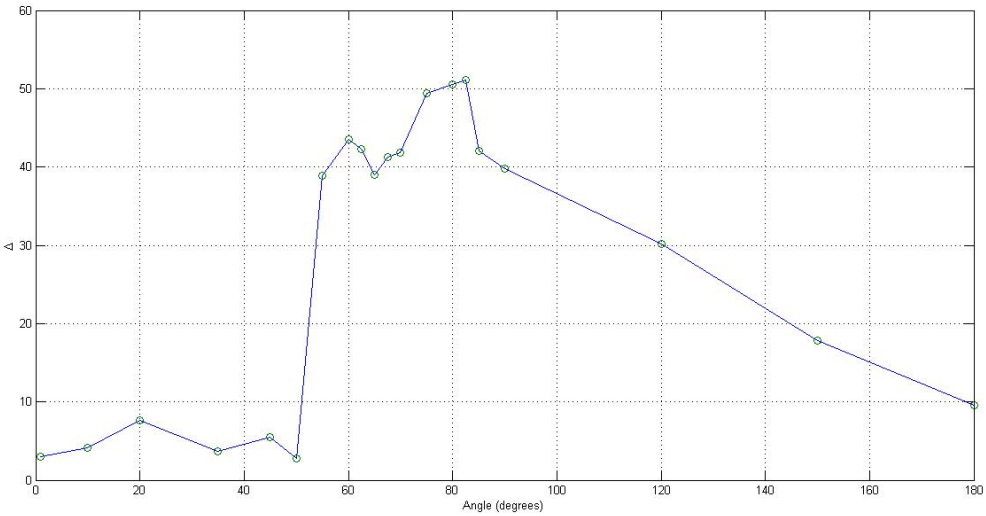

Figure 5.6: Δ versus actuator angle of application

Similarly to the previous section, the above-mention conclusions based on the drag coefficient are also supported by the velocity representation of the flow.

Four representative cases are here-after shown in order to grasp the behaviour of the flow in each angle region: $\theta = 82.5^{o}$, $\theta = 60^{o}$, $\theta = 50^{o}$, $\theta = 20^{o}$.

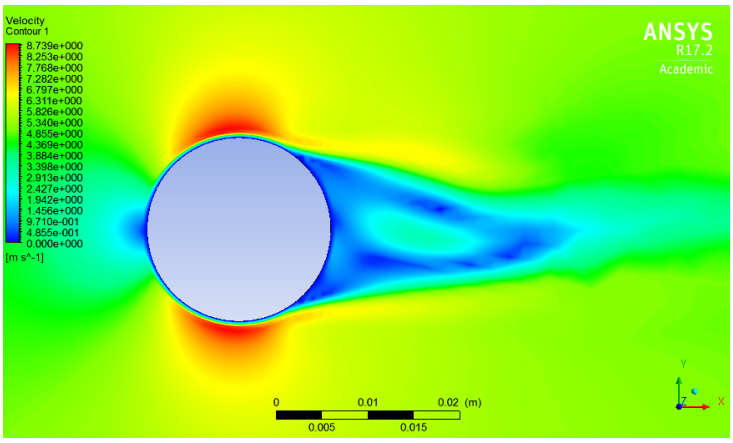

Figure 5.7: Velocity contours for $V_{\infty} = 5m/s$ and $\theta = 82.5^{o}$

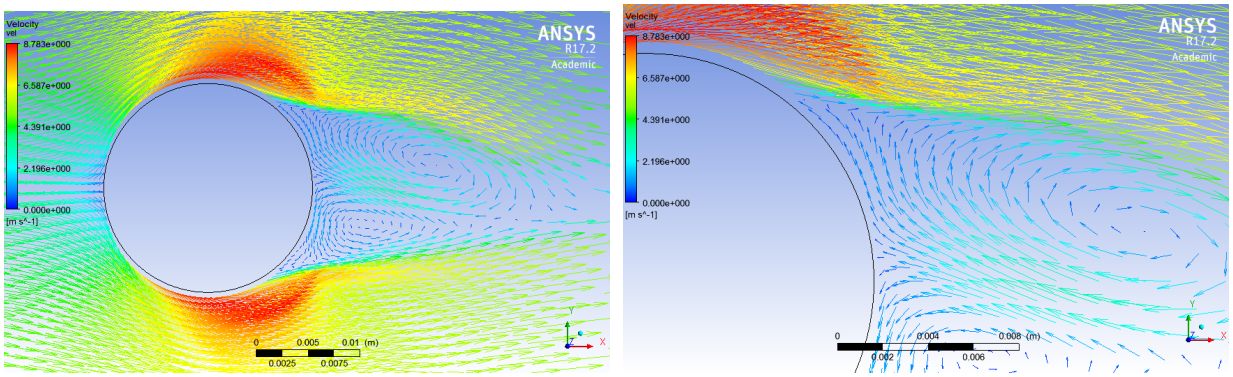

(a) Velocity vector representation

(b) Velocity vector representation zoom

Figure 5.8: Velocity vector representation for $V_{\infty} = 5m/s$ and $\theta = 82.5^{o}$

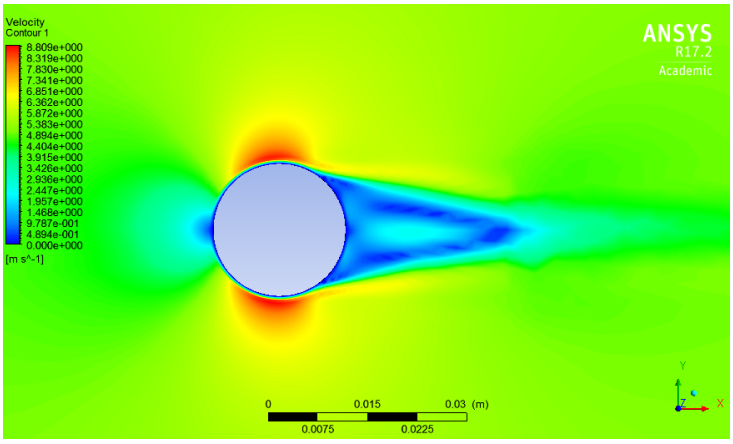

Figure 5.9: Velocity contours for $V_{\infty} = 5m/s$ and $\theta = 60^{o}$

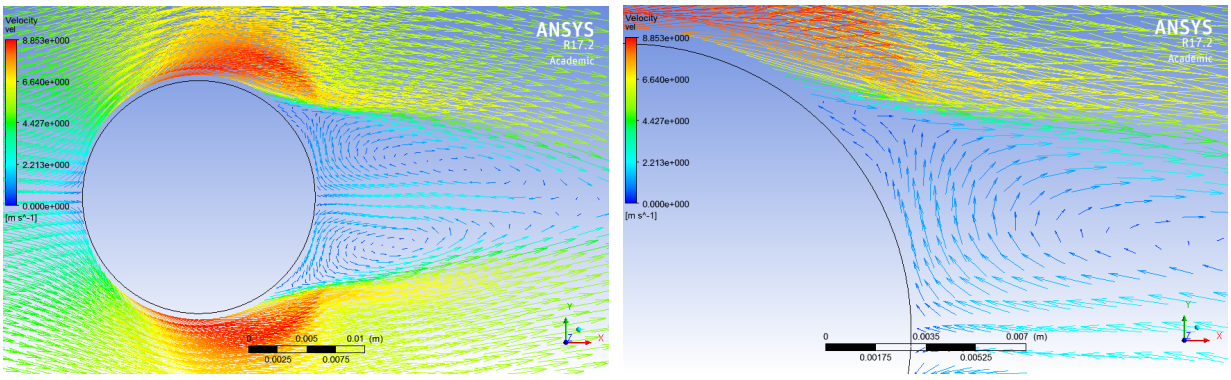

(a) Velocity vector representation

(b) Velocity vector representation zoom

Figure 5.10: Velocity vector representation for $V_\infty = 5m/s$ and $\theta = 60^o$

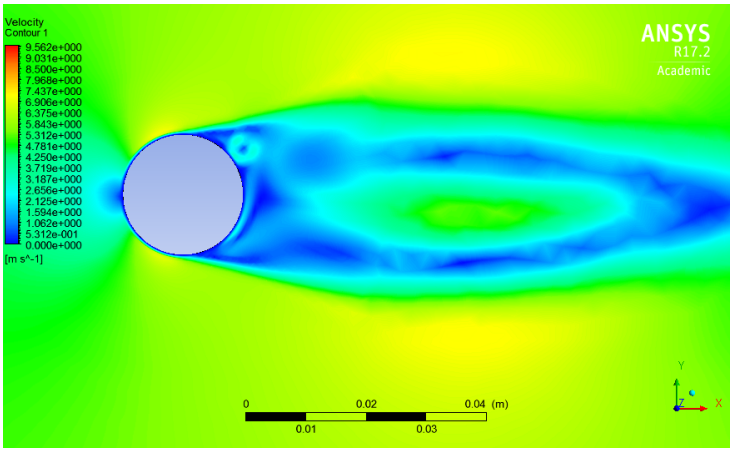

Figure 5.11: Velocity contours for $V_\infty = 5m/s$ and $\theta = 50^o$

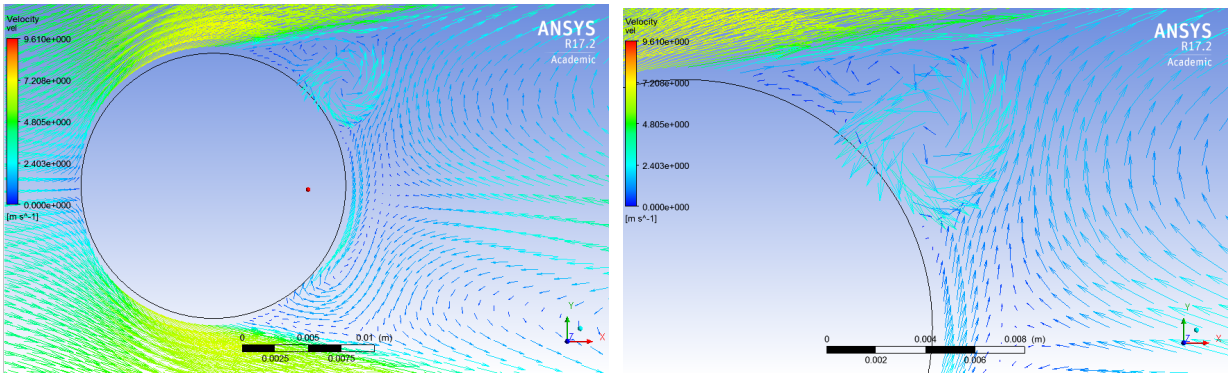

(a) Velocity vector representation

(b) Velocity vector representation zoom

Figure 5.12: Velocity vector representation for $V_\infty = 5m/s$ and $\theta = 50^o$

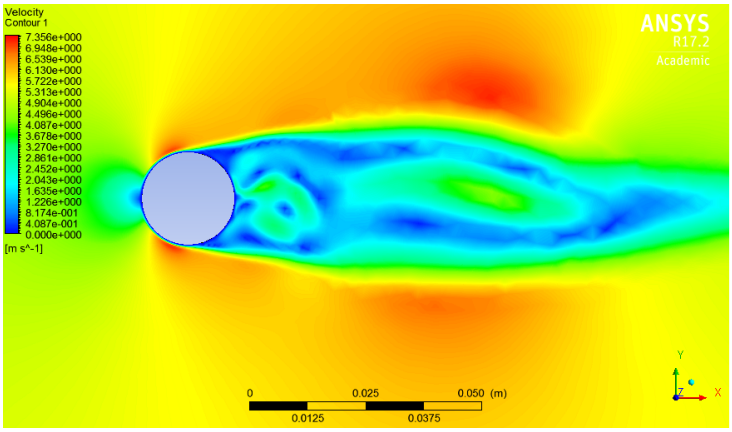

Figure 5.13: Velocity contours for $V_\infty = 5m/s$ and $\theta = 20^o$

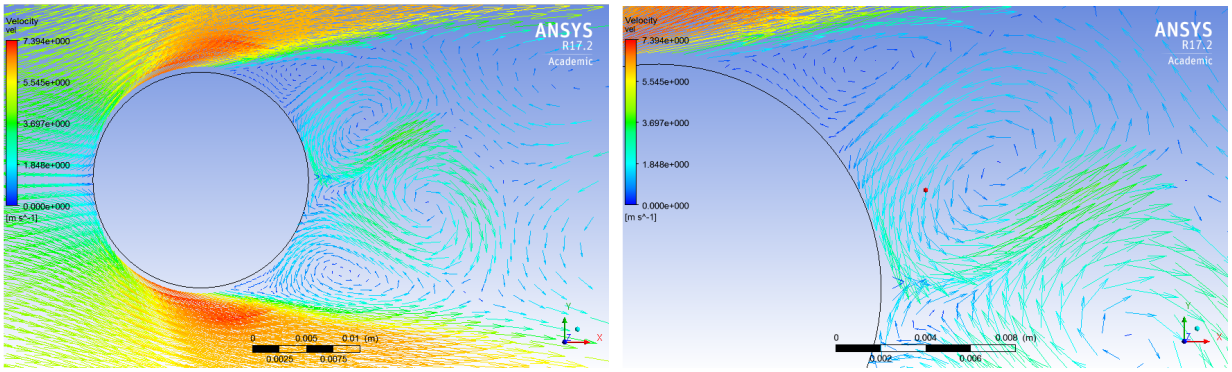

(a) Velocity vector representation

(b) Velocity vector representation zoom

Figure 5.14: Velocity vector representation for $V_\infty = 5m/s$ and $\theta = 20^o$

5.4 FFT for deeper understanding of the actuation

In this section, Fast Fourier Transform (FFT) is applied to the velocity evolution with time in three points placed at different distances from the cylinder: As shown in Figure 5.1 two points placed at $y = 0$, P1 at $x = D = 2cm$, P2 at at $x = 3D = 6cm$ and P3 placed at $y = D/2 = 1cm$ and $x = 6D = 12cm$. This last point is selected outside the zero-height line in order to obtain wider amplitude and lower noise in the results. This is done with two different Soloviev constants: $F_{Sol} = 0.005N/m$ and $F_{Sol} = 0.015N/m$. The study is performed for a free-steam velocity of $V_\infty = 5m/s$, which results on a Reynolds number $Re = 6800$, and an angle of application of $\theta = 70^o$. This configuration was selected based on the previous sections' results which suggest that the velocity and angle selected will provide representative and clear results.

Then, the results are compared with those obtained experimentally by L. Barbato, which are here again shown in Figure 5.15. Note that the Re number used was the same as in the present project.

In addition, the evolution of the velocity fluctuations, $V'(t)$ with actuators on and off is compared for a period of time at which both signals are periodically stable. The velocity fluctuation is the distance from the average value of the velocity ($\bar{V}$) to the total velocity ($V(t)$) at each instant of time. The resultant plot shows the velocity fluctuation centered at zero. $V'(t)$ is defined as follows:

$$V'(t) = V(t) - \bar{V}$$

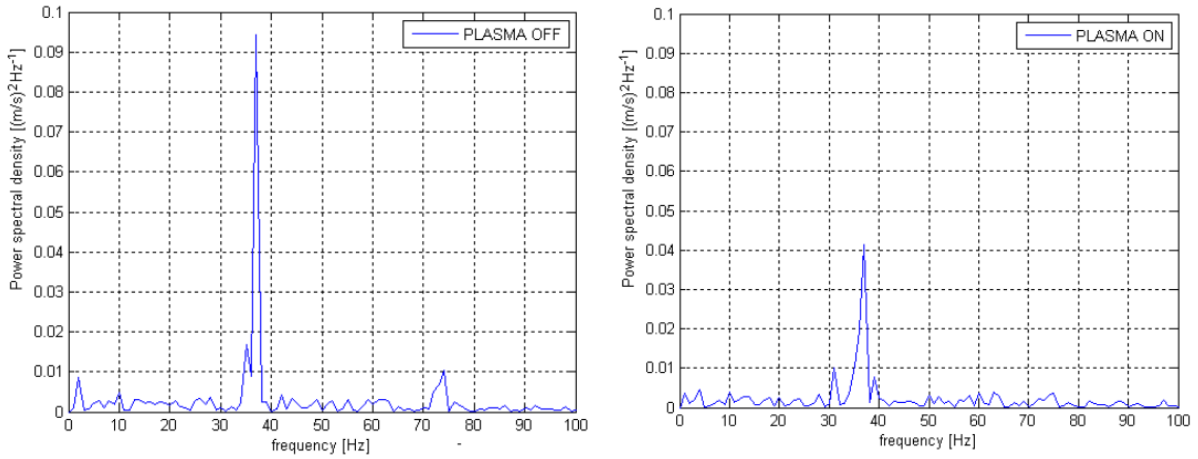

(a) Experimental FFT actuators OFF

(b) Experimental FFT actuators OFF

Figure 5.15: Experimental FFT with actuators on and off at $x = 6D$, $y = D/2$ and $Re = 6800$.

5.4.1 Soloviev force $F_{Sol} = 0.005$ N/m

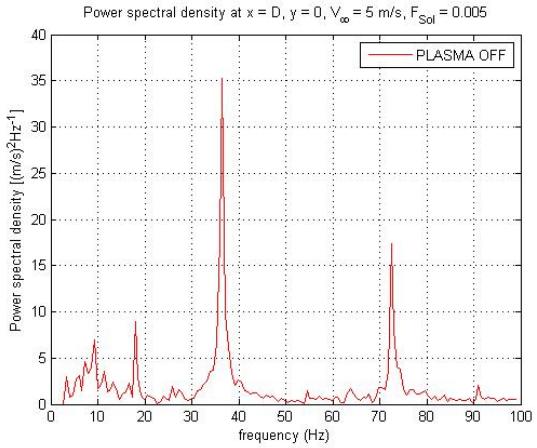

(a) FFT with actuators OFF at P_1

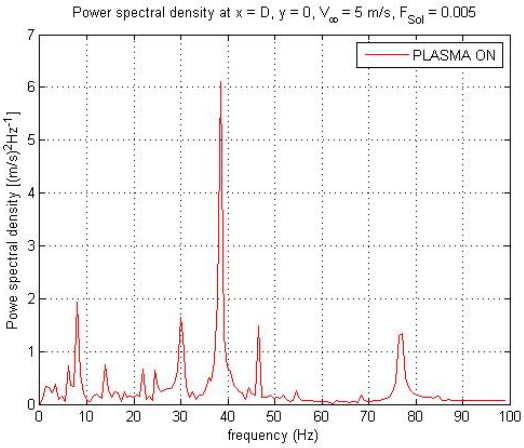

(b) FFT with actuators ON at P_1

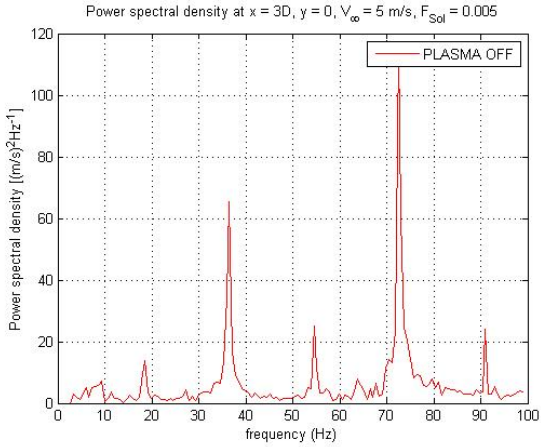

(c) FFT with actuators OFF at P_2

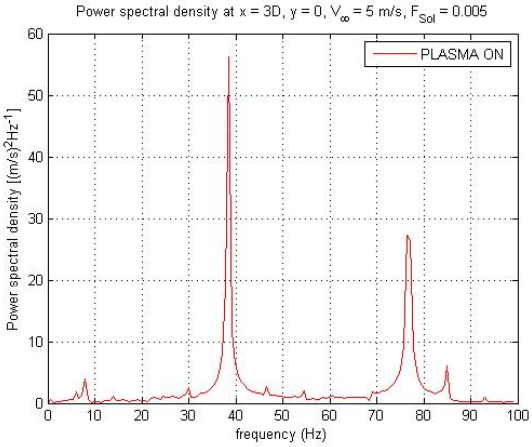

(d) FFT with actuators ON at P_2

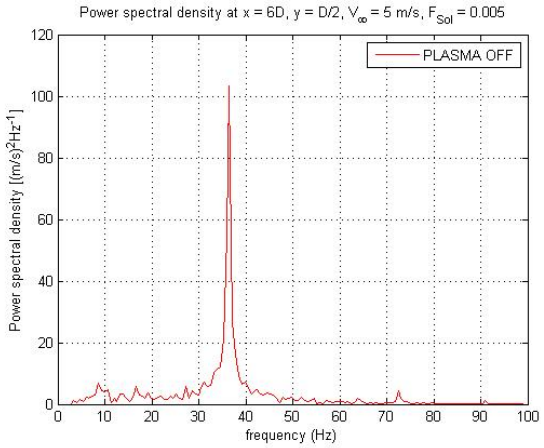

(e) FFT with actuators OFF at P_3

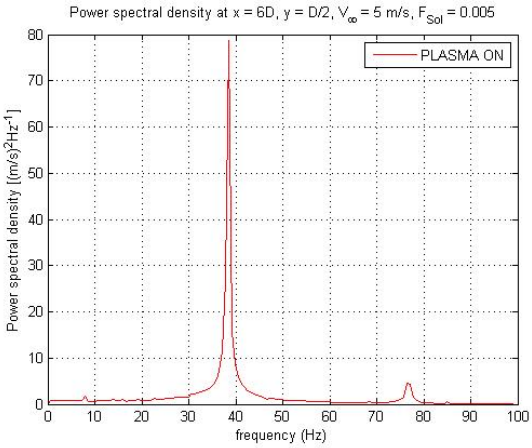

(f) FFT with actuators ON at P_3

Figure 5.16: FFT with actuators ON and OFF obtained in different points with $Re = 6800$

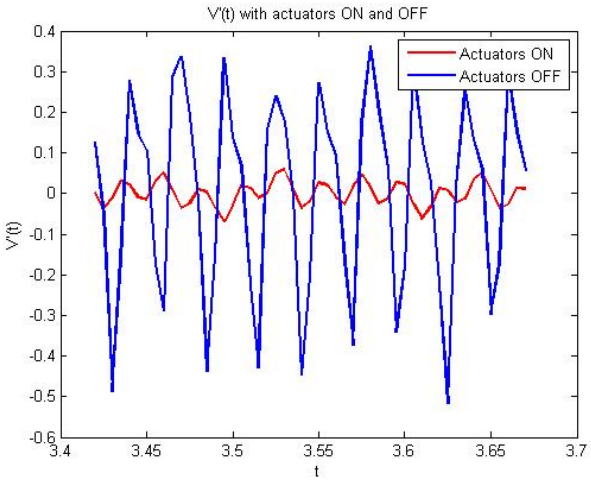

(a) $V'(t)$ evolution with actuators ON and OFF in point P1

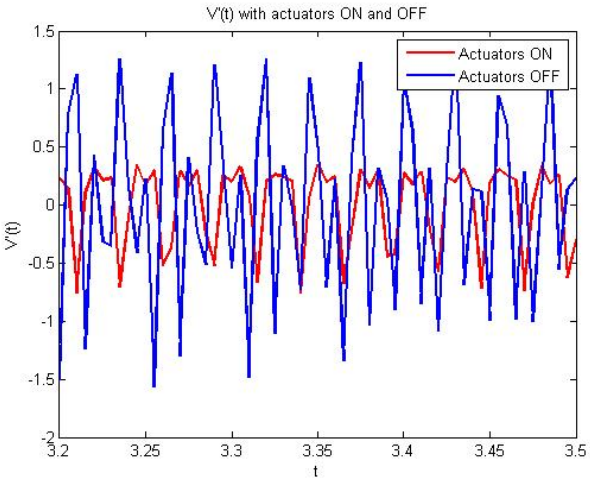

(b) $V'(t)$ evolution with actuators ON and OFF in point P1

Figure 5.17: $V'(t)$ evolution with actuators ON and OFF in points P1 and P2

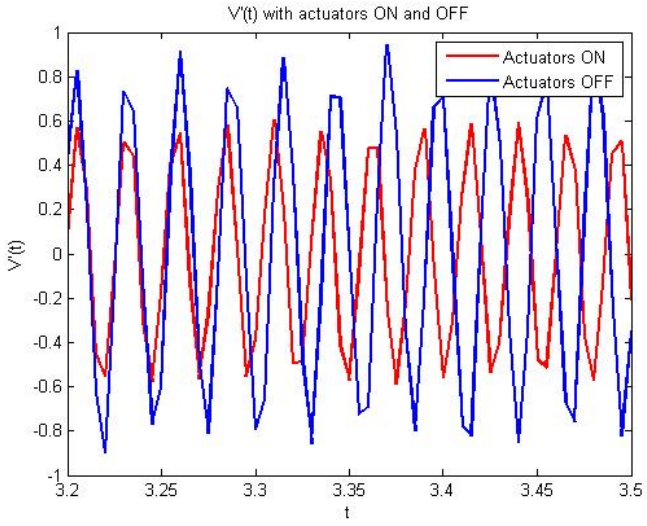

Figure 5.18: $V'(t)$ evolution with actuators ON and OFF in point P3

5.4.2 Soloviev force $F_{Sol} = 0.015$ N/m

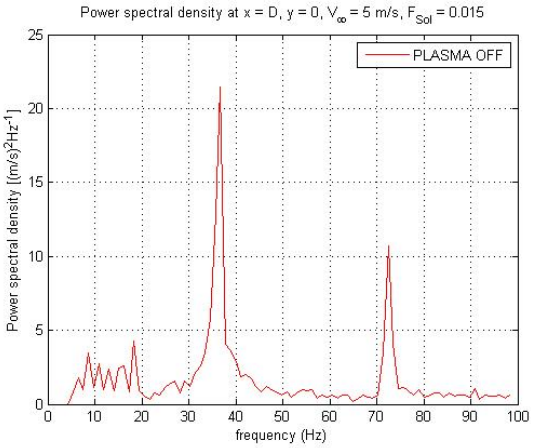

(a) FFT with actuators OFF at P_1

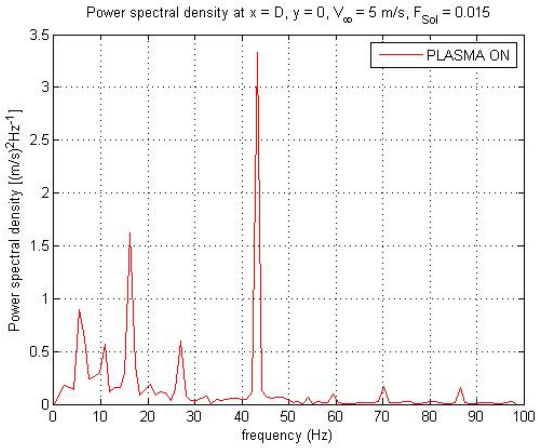

(b) FFT with actuators ON at P_1

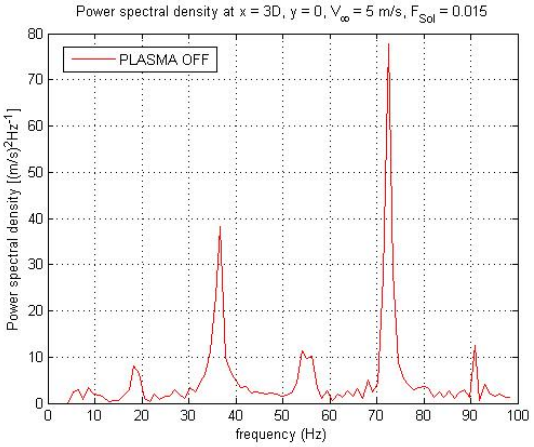

(c) FFT with actuators OFF at P_2

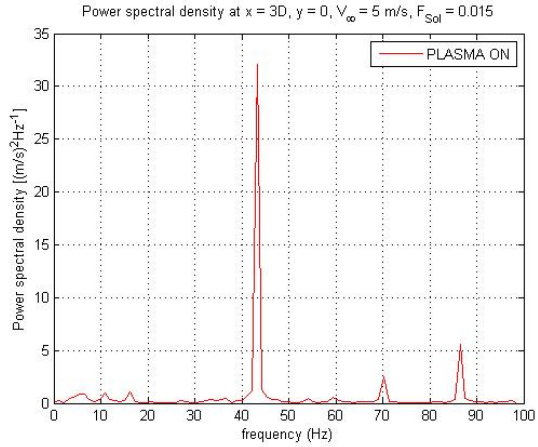

(d) FFT with actuators ON at P_2

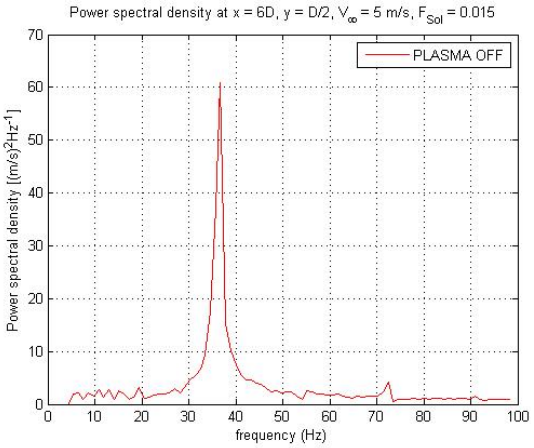

(e) FFT with actuators OFF at P_3

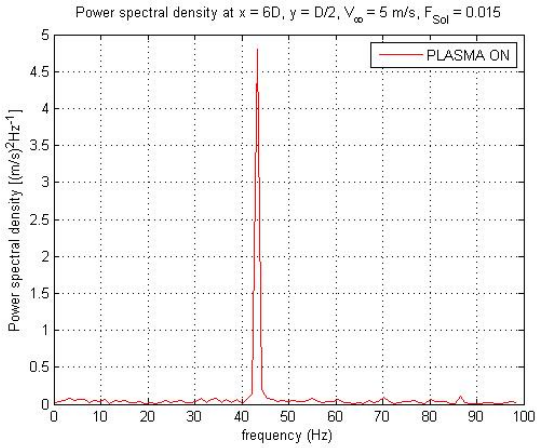

(f) FFT with actuators ON at P_3

Figure 5.19: Velocity representation for different velocities with actuators ON and OFF

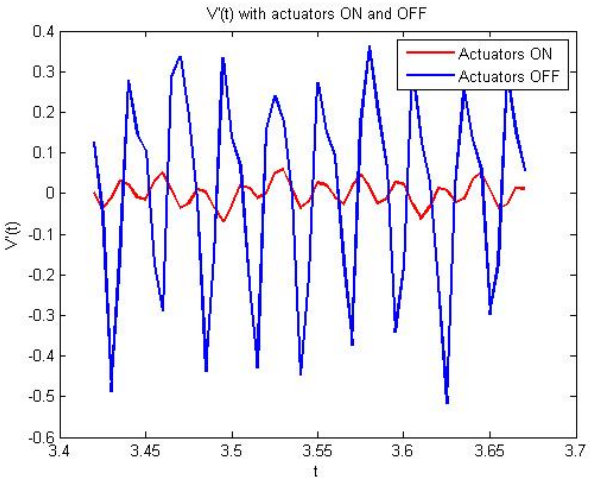

(a) $V'(t)$ evolution with actuators ON and OFF in point P1

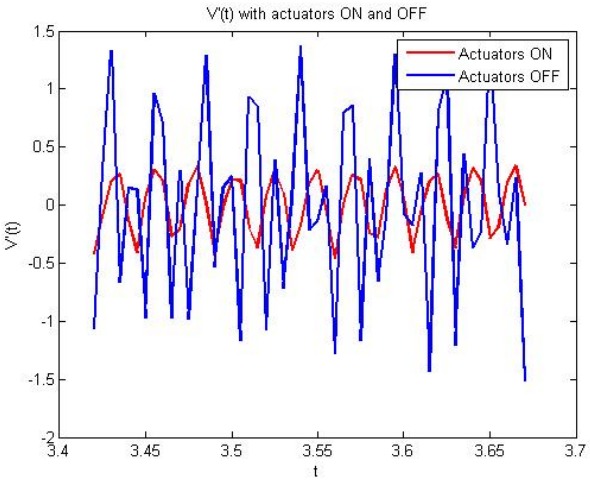

(b) $V'(t)$ evolution with actuators ON and OFF in point P2

Figure 5.20: $V'(t)$ evolution with actuators ON and OFF in points P1 and P2

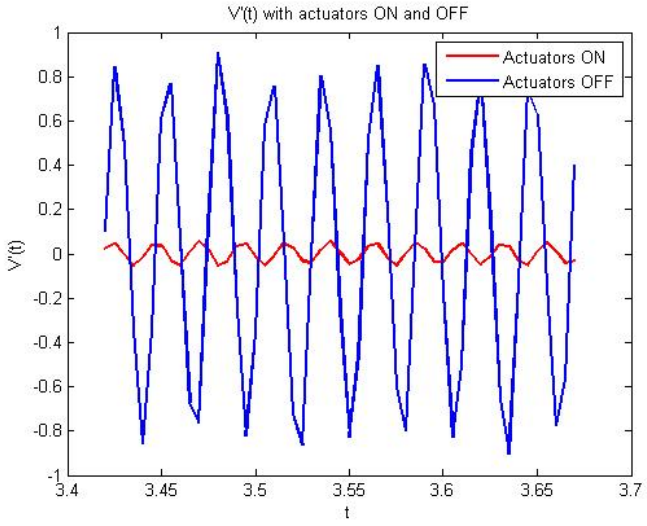

Figure 5.21: $V'(t)$ evolution with actuators ON and OFF in point P3

As can be seen in the previous Figures, the main effect of the actuators is exactly the same as the one obtained experimentally by L. Barbato. Figures 5.16 and 5.19 show a clear power spectral density attenuation when the actuators are activated. In addition, in Figures 5.17,5.18, 5.20 and 5.21, the amplitude of $V'(t)$ is reduced by the presence of the actuators.

Nevertheless, there exists a sift in frequency when the actuators are activated. It means that, in addition to the wake mitigation, the frequency of the Von Kármán instability is changed. This contradicts the results of L. Barbato that does not show any frequency variation. However, results holds consistency, as this frequency difference is higher the grater the value of the body force. This means that when $F_{Sol} = 0.015N/m$ the actuation is so strong that there is a higher injection of momentum that makes the velocity to considerably increase and consequently the instability frequency reaches greater values. When $F_{Sol} = 0.005N/m$, this effect is clearly attenuated, but still present. This explanation is consistent with the fact that L. Barbato' FFT does not show a frequency sift, as the actuation force introduced was weaker.

5.5 Turbulent Kinetic Energy (TKE)

In order to compare the turbulence present in the three points when the actuators are on and off for different values of the Soloviev constant, the Turbulent Kinetic Energy (TKE) is calculated. The procedure to obtain it was to calculate the y component of the velocity (v) from the x component (u) and the modulus ($\bar{V}$) directly extracted from Fluent with the following expression:

$$v(t) = \sqrt{\bar{V}(t)^2 - u(t)^2)}$$

Then, similarly to the previous section, the velocity fluctuation for each component is obtained:

$$u'(t) = u(t) - \bar{u}$$
$$v'(t) = v(t) - \bar{v}$$

Finally, the TKE is calculated as follows:

$$TKE = \frac{1}{2}\sqrt{\bar{u'^2} + \bar{v'^2}}$$

Results are shown in Table 5.1.

F_{Sol}	P_{1OFF}	P_{1ON}	P_{2OFF}	P_{2ON}	P_{3OFF}	P_{3ON}
0.005	0.2324	0.0841	0.4821	0.2815	0.3198	0.0993
0.015	0.2324	0.0439	0.4821	0.1849	0.3198	0.0315

Table 5.1: TKE at the three points for different body forces

It is observed that the turbulence is reduced when the actuators are activated. In addition, the greater the Soloviev constant, the lower the turbulence due to the increase on the actuation effect.

Chapter 6

Conclusion

Different innovative flow control methods and strategies are under investigation. Among them, Electro Hydrodynamic (EHD) actuators have called the attention in the past years because of their high performance and low power consumption. This project focus on the body force created by the EHD through the implementation of the Merged model. This model has shown in the past to achieve high fidelity to reality but it can be further investigated and improved. Two paths has been followed to that end:

- One path was the investigation of the effect of the parameters of the EHD body force model distribution on the resulting velocity profiles. This parameters can be tuned in order to obtain velocity profiles more faithful to reality. In addition, in order to properly place and rotate the force distribution model, the parameter y_{ref} was introduced in the formulation. This parameter, together with x_0 enables the distribution to be placed wherever wanted with no changes in the global force nor distribution.

- The other path was to implement the model as it is, this is, with the parameters suggested by the authors, for realistic situations. In particular, it has been considered the application of the model for wake mitigation of the flow past a cylinder. Following this line of investigation, several conclusions have been reached:

    1. Through the inspection of the drag coefficient reduction when actuators are activated, the evolution of the actuation effect with the free-stream velocity has been obtained for different values of the body force. This evolution includes the discovery of the limiting velocity for each case, this is, the velocity at which no significant actuation effect is achieved.

    2. The evolution of the actuation performance with the angle of application. This study includes the finding of the optimal angle where to place the actuators in order to obtain the maximum effect. Counter-intuitively, it has been also discovered that placing the actuator in the surface of the cylinder exposed to the incoming flow has a positive effect. The actuation performance in this cases is even better than when placing them in a range of small angles on the rear part

of the cylinder as these cases suffer the detrimental effect of a re-circulation bubble.

3. A deeper understanding of the actuation effect was achieved through the application of FFT to the time dependant evolution of the velocity in several points of the cylinder wake and for different values of the body force. The numerical results were compared with experimental ones, finding a high degree of agreement. As expected, the amplitude of the wake is reduced and the power spectral density is attenuated, which means that effectively, the wake instability is reduced.

4. The Turbulent Kinetic Energy (TKE) has been calculated for different points and body forces. As expected, the turbulence is reduced when actuators are activated and it is further attenuated the greater the body force is.

From all the points above-mentioned, it is clear that promising conclusions have been achieved regarding the potential of this model for flow control purposes. It has been proven to produce a wake instability reduction that improves the aerodynamic performance and a clear potential to mitigate the oscillation phenomena. This opens the perspective to investigate with this model the noise reduction demonstrated by V. Kozlov al.

Bibliography

[1] Lorena del Amo Martín. Flow control using dbd plasma actuators: experimental investigation. B.S. thesis, 2015.

[2] Luigi Barbato. Boundary layer mitigation by means of plasma actuators. B.S. thesis, 2010.

[3] Robert D Blevins. Flow-induced vibration. 1990.

[4] Romain Futrzynski. *Drag reduction using plasma actuators*. PhD thesis, KTH Royal Institute of Technology, 2015.

[5] Balaji Jayaraman and Wei Shyy. Modeling of dielectric barrier discharge-induced fluid dynamics and heat transfer. *Progress in Aerospace Sciences*, 44(3):139–191, 2008.

[6] Antonio L. Sánchez. Fluid mechanics: an introduction and some relevant application. Academic notes, 2011.

[7] Alexandre Likhanskii, Mikhail Shneider, Dmitry Opaits, Richard Miles, and Sergey Macheret. Numerical modeling of dbd plasma actuators and the induced air flow. In *38th AIAA Plasmadynamics and Lasers Conference In conjunction with the 16th International Conference on MHD Energy Conversion*, page 4533, 2007.

[8] Edgar Martín Nieto. Boundary layer control by means of dbd plasma actuators. B.S. thesis, 2016.

[9] Clark Blanchard Millikan et al. Aerodynamics of the airplane. 1946.

[10] J Reece Roth. Aerodynamic flow acceleration using paraelectric and peristaltic electrohydrodynamic effects of a one atmosphere uniform glow discharge plasma. *Physics of plasmas*, 10(5):2117–2126, 2003.

[11] W Shyy, B Jayaraman, and A Andersson. Modeling of glow discharge-induced fluid dynamics. *Journal of applied physics*, 92(11):6434–6443, 2002.

[12] Kunwar Pal Singh and Subrata Roy. Force approximation for a plasma actuator operating in atmospheric air. *Journal of Applied Physics*, 103(1):013305, 2008.

[13] VR Soloviev. Analytical estimation of the thrust generated by a surface dielectric barrier discharge. *Journal of Physics D: Applied Physics*, 45(2):025205, 2011.

[14] VR Soloviev and VM Krivtsov. Surface barrier discharge modelling for aerodynamic applications. *Journal of Physics D: Applied Physics*, 42(12):125208, 2009.

[15] Flint Thomas, Alexey Kozlov, and Thomas Corke. Plasma actuators for bluff body flow control. In *3rd AIAA Flow Control Conference*, page 2845, 2006.